

Supplementary Information for

Laser-Induced High-Entropy Alloys as Long-Duration Bifunctional Electrocatalysts for Seawater Splitting

Yunchao Xie^{1#}, Shichen Xu^{2#}, Andrew C. Meng³, Bujingda Zheng¹, Zhenru Chen¹, James M. Tour^{2, 4, 5, 6*}, and Jian Lin^{1*}

¹Department of Mechanical and Aerospace Engineering

³Department of Physics and Astronomy

University of Missouri, Columbia, MO 65201, United States

²Department of Chemistry

⁴Department of Materials Science and NanoEngineering

⁵Department of Computer Science Engineering

⁶NanoCarbon Center and the Rice Advanced Materials Institute

Rice University, 6100 Main Street, Houston, Texas 77005, United States

#Equal contribution

*Email: LinJian@missouri.edu; tour@rice.edu.

Supplementary Notes

Note S1: The atomic size difference (δ), electronegativity difference ($\Delta\chi$), mixing enthalpy (ΔH_{mix}), mixing entropy (ΔS_{mix}), mixing valence electron concentration (VEC_{mix}), mixing melting temperature (T_{mix}) and lattice constant of HEA are calculated according to the following equations:

$$\delta = \sqrt{\sum_{i=1}^n c_i \left(1 - \frac{r_i}{\bar{r}}\right)^2} \quad (1)$$

$$\bar{r} = \sum_{i=1}^n c_i r_i \quad (2)$$

$$\Delta\chi = \sqrt{\sum_{i=1}^n c_i (\chi_i - \bar{\chi})^2} \quad (3)$$

$$\bar{\chi} = \sum_{i=1}^n c_i \chi_i \quad (4)$$

$$\Delta S_{mix} = -R \sum_{i=1}^n c_i \ln(c_i) \quad (5)$$

$$\Delta H_{mix} = \sum_{i=1, j \neq i}^n \Omega_{ij} c_i c_j \quad (6)$$

$$\Omega_{ij} = 4 \Delta_{mix}^{AB} \quad (7)$$

$$VEC_{mix} = \sum_{i=1}^n c_i (VEC)_i \quad (8)$$

$$T_{mix} = \sum_{i=1}^n c_i (T_m)_i \quad (9)$$

$$a_{mix} = 2\sqrt{2\bar{r}} \quad (10)$$

where c_i , r_i , χ_i , $(VEC)_i$, and $(T_m)_i$ are the atomic percentage, atomic radius, electronegativity, valence electron concentration, and melting temperature of the i th element. R refers to gas constant, while Δ_{mix}^{AB} is the mixing enthalpy of binary alloys. It is reported that δ , ΔH_{mix} , ΔS_{mix} and VEC_{mix} should fall within the range of $0 \leq \delta \leq 8.5$, $-22 \leq \Delta H_{mix} \leq 7$, $11 \leq \Delta S_{mix} \leq 19.5$, and $VEC_{mix} \geq 8$, respectively, to form single-phase solid solution.

Note S2: Determination of the concentration of metal species using the digestion technique.

Standard solution preparation

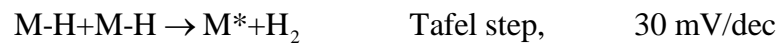
Standard solutions including Fe, Co, Ni, Cr, and Ru were prepared by mixing metal chlorides with concentration of 1000 mg/L. Then, the standard solutions were diluted with 2 wt% hydrochloric acid to various concentrations ranging from 1 ppb to 100 ppb, utilizing gallium (Ga) as the internal standard.

Determination of metal species

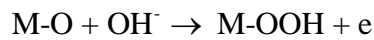
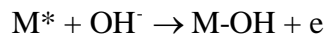
To begin, four pieces of carbon paper with HEA NPs were immersed in 3 mL of concentrated HCl and 1 mL of concentrated HNO₃ for 2 hours. Following this, super-pure water was added to the solution to achieve a total mass of 50 g. After removing the carbon paper through filtration, the resulting solution was further diluted by a factor of 100. The measurement was conducted using an ICP-MS system, specifically the PerkinElmer Nexion 300 ICP-MS. Prior to the measurement, the ICP-MS equipment was meticulously calibrated.

Note S3: Electrocatalytic mechanism of HER and OER under an alkaline electrolyte.

HER in alkaline electrolyte:



OER in alkaline electrolyte:



Note S4: Calculation of turnover frequency (TOF)

Turnover frequency (TOF) was calculated according to the following equation.

$$\text{TOF} = \frac{\text{total number of hydrogen turnovers} \times J}{\text{total number of active sites} \times \text{ECSA}}$$

Total number of active sites ($N_{\text{active sites}}$) is determined using the following equation:

$$\begin{aligned} N_{\text{active sites}} &= \left(\frac{4 \text{ atom per unit cell}}{a_{\text{mix}}^3 \text{ per unit cell}} \right)^{2/3} \\ &= \frac{4^{2/3}}{a^2} \times 10^{14} \left(\frac{\text{atoms}}{\text{cm}_{\text{real}}^2} \right) \end{aligned}$$

Total number of hydrogen turnover (N_{H_2}) at current density of J is determined using the following equation:

$$\begin{aligned} N_{H_2} &= \left(\frac{1 \text{ C/s}}{1000 \text{ mA}} \right) \times \left(\frac{1 \text{ mol e}}{96485.3 \text{ C}} \right) \times \left(\frac{1 \text{ mol H}_2}{2 \text{ mol e}} \right) \times \left(\frac{6.022 \times 10^{23} \text{ H}_2/\text{mol}}{1 \text{ mol H}_2} \right) \times J \left(\frac{\text{mA}}{\text{cm}^2} \right) \\ &= 3.121 \times 10^{15} \left(\frac{\text{H}_2/\text{s}}{\text{mA}} \right) \times J \left(\frac{\text{mA}}{\text{cm}^2} \right) \end{aligned}$$

Total number of oxygen turnover (N_{O_2}) at current density of J is determined using the following equation:

$$\begin{aligned} N_{H_2} &= \left(\frac{1 \text{ C/s}}{1000 \text{ mA}} \right) \times \left(\frac{1 \text{ mol e}}{96485.3 \text{ C}} \right) \times \left(\frac{1 \text{ mol O}_2}{4 \text{ mol e}} \right) \times \left(\frac{6.022 \times 10^{23} \text{ O}_2/\text{mol}}{1 \text{ mol O}_2} \right) \times J \left(\frac{\text{mA}}{\text{cm}^2} \right) \\ &= 1.560 \times 10^{15} \left(\frac{\text{H}_2/\text{s}}{\text{mA}} \right) \times J \left(\frac{\text{mA}}{\text{cm}^2} \right) \end{aligned}$$

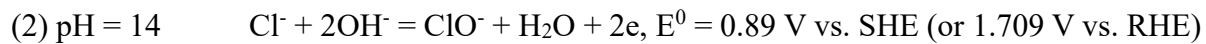
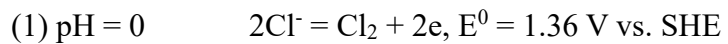
Finally, the TOF_{HER} and TOF_{OER} are calculated as follow:

$$\begin{aligned}
\text{TOF}_{\text{HER}} &= \frac{3.121 \times 10^{15} \left(\frac{\text{H}_2/\text{s}}{\text{mA}} \right) \times J \left(\frac{\text{mA}}{\text{cm}^2} \right)}{\frac{4^{2/3}}{a^2} \times 10^{14} \left(\frac{\text{atoms}}{\text{cm}^2_{real}} \right) \times \text{ECSA}_{\text{HER}} \left(\text{cm}^2 \right)} \\
&= \frac{12.386 \times a^2 \times J}{\text{ECSA}_{\text{HER}}} \left(\text{s}^{-1} \right) \\
\text{TOF}_{\text{OER}} &= \frac{1.560 \times 10^{15} \left(\frac{\text{O}_2/\text{s}}{\text{mA}} \right) \times J \left(\frac{\text{mA}}{\text{cm}^2} \right)}{\frac{4^{2/3}}{a^2} \times 10^{14} \left(\frac{\text{atoms}}{\text{cm}^2_{real}} \right) \times \text{ECSA}_{\text{OER}} \left(\text{cm}^2 \right)} \\
&= \frac{6.191 \times a^2 \times J}{\text{ECSA}_{\text{OER}}} \left(\text{s}^{-1} \right)
\end{aligned}$$

Note S5: Hypochlorite production at an alkaline seawater electrolyte.

The chemistry of chlorine in aqueous environments encompasses an intricate array of potential reactions, which are contingent upon the pH and concentration of chloride ions present.^{1, 2} The dominance of the chlorine evolution reaction is observed when the pH is below 3. The formation of hypochlorous acid takes precedence in the pH range of 3 to 7.5. Additionally, the generation of hypochlorite becomes prominent at pH values exceeding 7.5.

At extreme pH values, two chlorine oxidation reactions can happen:



Note S6: Detailed discussion about the feasibility and advancements of using seawater as feedstock for hydrogen production.

First, proton exchange membrane water electrolysis (PEMWE) is widely recognized and extensively deployed globally due to its exceptional catalytic activity and durability. However, the limited availability of electrode materials (such as Pt/C for the hydrogen evolution reaction and IrO₂ for the oxygen evolution reaction) and significant freshwater scarcity in many regions pose substantial challenges to PEMWE's further expansion. Given these limitations, anion exchange membrane water electrolysis (AEMWE) has garnered significant attention, as it enables the use of cost-effective transition metal catalysts, membranes, ionomers, and construction materials. This leads to significant cost reductions, particularly in terms of capital investment, operation, and maintenance expenses.

Second, the United States has launched seven Hydrogen Hubs, a \$7 billion initiative aimed at accelerating the development and deployment of hydrogen technologies as a central component of the nation's clean energy transition (**Fig. N1**). Supported by the U.S. Department of Energy, these hubs are intended to foster regional hydrogen production and use across various industries and applications. Each hub focuses on different technologies, resources, and applications to develop a robust hydrogen economy. Approximately two-thirds of the total investment is allocated to electrolysis-based green hydrogen production within these H2Hubs. Four of these hubs are in the coastal regions: California Hydrogen Hub (ARCHES), Gulf Coast Hydrogen Hub (HyVelocity), Mid-Atlantic Hydrogen Hub (MACH2), and Pacific Northwest Hydrogen Hub (PNWH2). For a state like California, which faces significant freshwater shortages and is heavily dependent on

importing water from neighboring regions, utilizing freshwater as feedstock for hydrogen production is highly impractical. Moreover, approximately 40% of the state's total water resources are already allocated to agricultural irrigation. Given the persistent scarcity of freshwater, producing green hydrogen from seawater using AEMWE could be a strategic focus to alleviate pressure on existing freshwater supplies.



Figure N1. The map of selected regional clean hydrogen hubs (<https://www.energy.gov/oced/regional-clean-hydrogen-hubs-selections-award-negotiations>).

Third, although alkaline seawater electrolysis is still in its early stages and faces skepticism,³⁻⁹ several research groups have made pioneering advancements in enhancing corrosion resistance, reducing energy requirements, and boosting catalytic activity. Qiao and coworkers manipulated the local reaction environment for seawater electrolysis by introducing a Lewis acid layer of CrO_x over transitional metal oxides (**Fig. N2a** and **N2b**).¹⁰ The Lewis acid layer significantly enhance water dissociation and captures hydroxyl anions, thus facilitating HER kinetics while also prevent unwanted precipitation. The flow-type electrolyzer afforded a good stability up to 100 h at 500 mA/cm² and exhibited an industrially required current density of 1.0 A/cm² at 1.87 V and 60 °C.

Another study adopted a similar strategy to enhance catalytic activity by incorporating a protective V₂O₃ layer, which improves interfacial conductivity, water adsorption, and hydrogen desorption, significantly boosting catalytic performance.¹¹ The Lewis acid properties of the V₂O₃ layer modulate the local reaction environment at the catalytic sites. Furthermore, the captured excess OH⁻ repels negatively charged Cl⁻, reducing its attack on the primary active site and preventing salt precipitation, leading to remarkable long-term stability.

Another group employed effective strategies of structural modulation and heterostructure design to simultaneously mitigate anode corrosion caused by Cl⁻ ions and boost OER activity (**Fig. N2c**).¹² The as-synthesized earth-abundant layered double hydroxide electrocatalyst that sustains stable electrolysis of seawater over 2,800h under an ultra-high current density of 1.25 A/cm². It is inferred that structural modulation through carbonate intercalation enhances Cl⁻ corrosion resistance and operational durability, while surface anchoring of graphene quantum dots induces Coulomb repulsion of Cl⁻ from the surface-active sites, further improving stability.

To reduce the energy requirements caused by the sluggish oxygen evolution reaction, Zhou et al. developed a hybrid seawater electrolyzer that combines thermodynamically favorable sulfion oxidation with cathodic seawater reduction (**Fig. N2d**).¹³ This hybrid system demonstrates exceptional durability, operating for 504 hours at a current density of 100 mA/cm². It achieves a lower power consumption of 1.2 kWh m⁻³ H₂, representing a reduction of more than 67.9% in power consumption compared to conventional alkaline seawater electrolyzer systems.

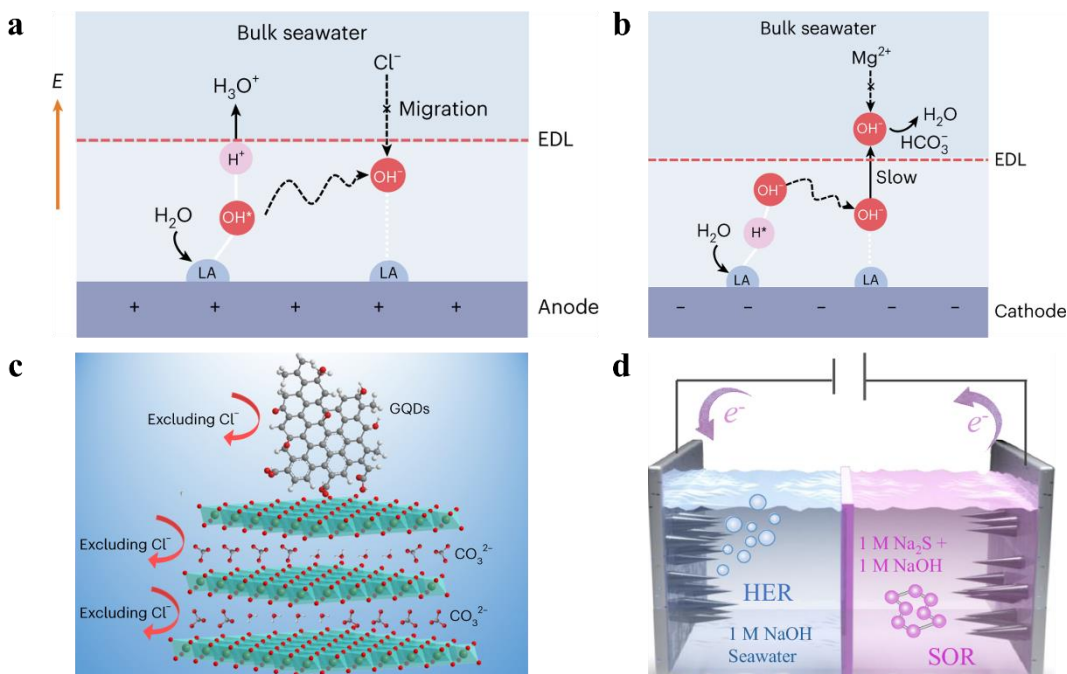


Figure N2. Schematic diagram of local alkaline microenvironment generation on (a) Lewis acid-modified anode, which facilitates OER and inhibits chlorine chemistry; (b) Lewis acid-modified cathode, which facilitates HER and prevents precipitate formation.¹⁰ Reproduced with permission from Ref¹⁰, Copyright 2023 Springer Nature. (c) Schematic illustration of electrocatalyst against Cl^- corrosion in seawater.¹² Reproduced with permission from Ref¹², Copyright 2024 Springer Nature. (d) Schematic diagram of the hybrid seawater electrolyzer system using bifunctional electrode in 1 M NaOH seawater for hydrogen evolution reaction and in 1 M Na_2S + 1 M NaOH for sulfion oxidation reaction (right).¹³ Reproduced under a Creative Commons CC BY license from Ref¹³, Copyright 2024 Spring Nature.

Fourth, pilot-scale and full-scale deployments of seawater electrolysis have been successfully demonstrated. Xie and colleagues developed a pilot-scale direct seawater electrolysis system that achieved stable operation at a current density of 250 mA/cm^2 for approximately 3,200 hours under practical application conditions, without any failure (**Fig. N3a**).¹⁴ This innovative system

incorporates hydrophobic porous waterproof breathable membrane and a self-dampening electrolyte, featuring a higher self-driven water migration rate, 100% ion-blocking efficiency, and excellent antifouling capability. Subsequently, Xie's team, in collaboration with industry partners, developed the world's first full-scale offshore wind-powered in-situ seawater electrolysis system that operated continuously and stably for over 240 hours (**Fig. N3b**).¹⁵ The system achieved a hydrogen production rate of $1.2 \text{ Nm}^3 \text{ H}_2/\text{h}$ with technical cost of \$1.5 – 2.3/kg H₂, a Faradaic efficiency of nearly 100% and hydrogen purity of 99.99 %.

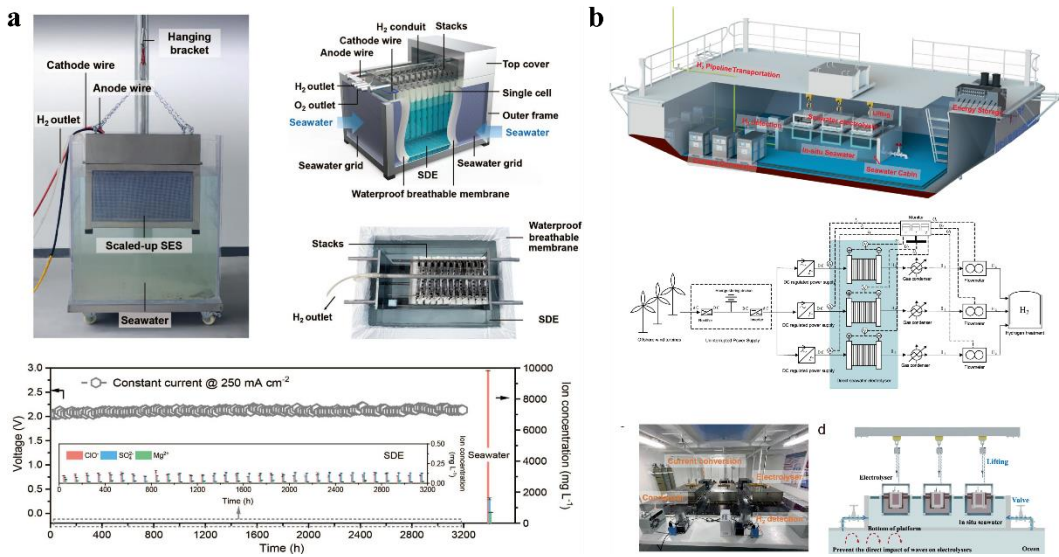


Figure N3. (a) Pilot-scale¹⁴ and (b) Full-scale¹⁵ deployment of seawater electrolysis system. Reproduced with permission from Ref ¹⁴, Copyright 2022 Springer Nature. Reproduced under a Creative Commons CC BY license from Ref ¹⁵, Copyright 2024 Spring Nature.

Fifth, seawater electrolysis complements rather than replaces PEM or AEM electrolysis, particularly in coastal regions with freshwater scarcity. The hydrogen demand in U.S. is projected to reach 10 million metric tons by 2030 and 50 million metric tons by 2050. Although 9 kg of water is theoretically required to produce 1 kg of H₂, actual water consumption for centralized electrolysis increases to 30.2 kg per kg of H₂ produced due to water demineralization.¹⁶ Currently,

electrolysis accounts for a smaller share of hydrogen production in the U.S., but it is expected to grow substantially as the country transitions to green hydrogen. Assuming water electrolysis accounts for 30% of the hydrogen demand, the projected water usage for electrolysis in the U.S. by 2050 could reach 453 million metric tons (**Fig. N4**). Therefore, developing seawater electrolysis as a complementary technology is essential to balance water use between human consumption and hydrogen production, ensuring sustainability in water-scarce areas.

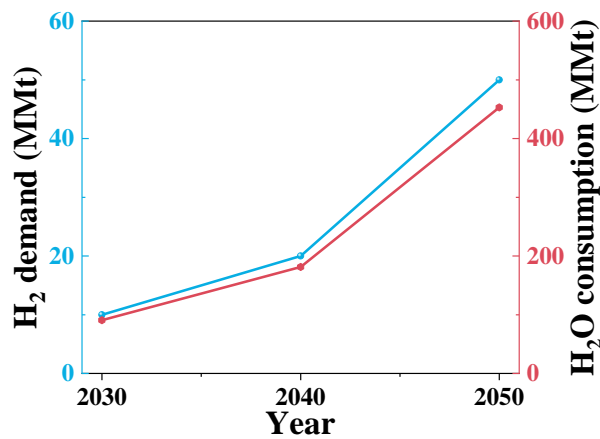


Figure N4. Planned clean hydrogen demand and the requirement amount of water consumption.

Finally, despite significant progress, seawater electrolysis remains far from achieving full acceptance and large-scale deployment. Continued efforts are needed to optimize critical components such as electrodes, electrolytes, anodic chlorine chemistry, and electrolyzer configurations. Additionally, the design and construction of innovative electrolyzers are essential to improve system performance and durability. By advancing the development of reliable and efficient seawater electrolysis technologies, it is anticipated to unlock the immense potential of the world's oceans as a source of clean and sustainable energy, contributing to global efforts in addressing climate change and reducing dependence on fossil fuels.

Note S7: Faradaic efficiency of HER and OER.

Both H₂ and O₂ gas produced at the cathode and anode were separately collected by the drainage gas collection method. The Faradaic efficiency (η) of HER and OER were evaluated by the following equations:

$$n = \frac{N}{N_A} = \frac{V}{V_m} = \frac{Q}{Z \times F}$$

$$\eta = \frac{n_{\text{exp}}}{n_{\text{theo}}} \times 100 = \frac{\frac{V_{\text{exp}}}{V_m}}{\frac{Q}{Z \times F}} = \frac{Z \times F \times V_{\text{exp}}}{Q \times V_m}$$

where, n is the molar amount of H₂/O₂ (mol), N is the number of particles, N_A is Avogadro constant, V is the volume of H₂/O₂ (L), V_m is the molar volume of gas (22.4 L/mol), Q is the quantity of electric charge (C), F is Faraday constant (96485.33 C/mol), Z is the number of transferred electrons ($Z = 2$ for H₂ and 4 for O₂).

Note S8: Determination of active chlorine (hypochlorite, ClO^-).

Chemicals. disodium phosphate dodecahydrate ($\text{Na}_2\text{HPO}_4 \cdot 12\text{H}_2\text{O}$, Sigma), potassium phosphate monobasic (KH_2PO_4 , Sigma), ethylenediaminetetraacetic acid disodium (EDTA-2Na, Sigma), hydrochloric acid (HCl, Fisher), sodium hypochlorite (NaClO , Fisher), N, N-diethyl-p-phenylenediamine sulfate (DPD, Fisher).

Phosphate buffer solution (PBS, pH = 6.5). Phosphate buffer solution was made by dissolving 30.27 g of $\text{Na}_2\text{HPO}_4 \cdot 12\text{H}_2\text{O}$, 23 g of KH_2PO_4 and 0.4 g of EDTA-2Na in 500 mL DI H_2O .

Determination of active chlorine species. The concentration of hypochlorite (ClO^-) was determined by colorimetric method. In detail, 1 mL of the electrolyte was first mixed with 0.5 mL of 2 M HCl solution. Subsequently, 0.25 mL of phosphate buffer and 0.25 mL of DPD were added to the solution, and the mixture was thoroughly shaken until the appearance of pink color. Finally, the absorbance of the resulting pink solution at 550 nm was measured by a UV-Vis spectrophotometer (PerkinElmer Lambda 35).

Supplementary Figures

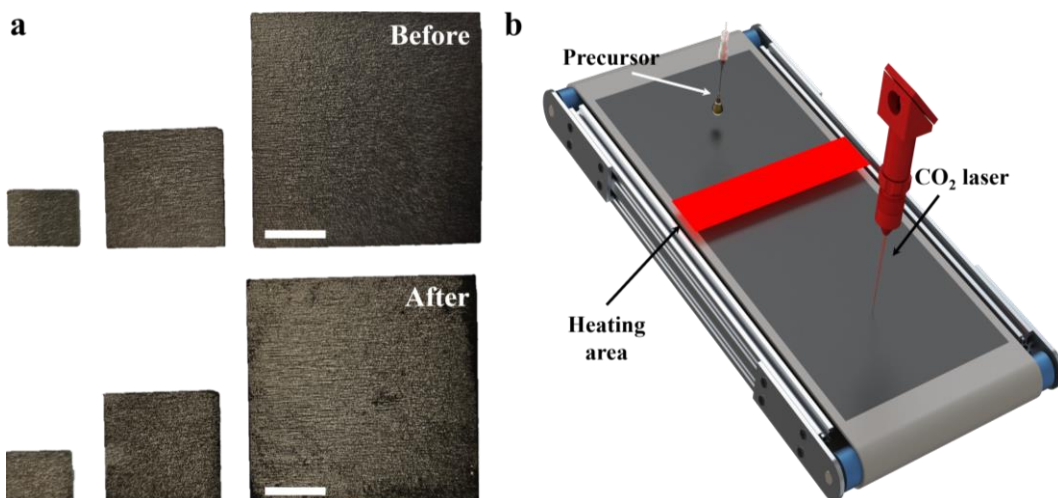


Figure S1. (a) Digital photos of FeNiCoCrRu HEA on carbon papers with different sizes ranging from 1.2 cm² to 16 cm² before and after laser induction. Scale bar: 1 cm. (b) Schematic showing continuous, scalable production of HEA NPs on carbon paper enabled by CO₂ laser induction deployed with spray coating, top heating, and a roll-to-roll apparatus.

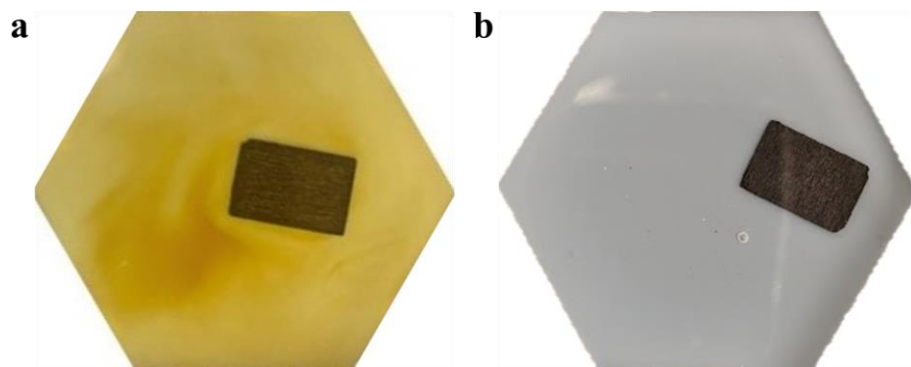


Figure S2. Photographs showing the color changes over (a) FeNiCoCrRu-NSC and (b) FeNiCoCrRu upon immersing in deionized water after laser induction.

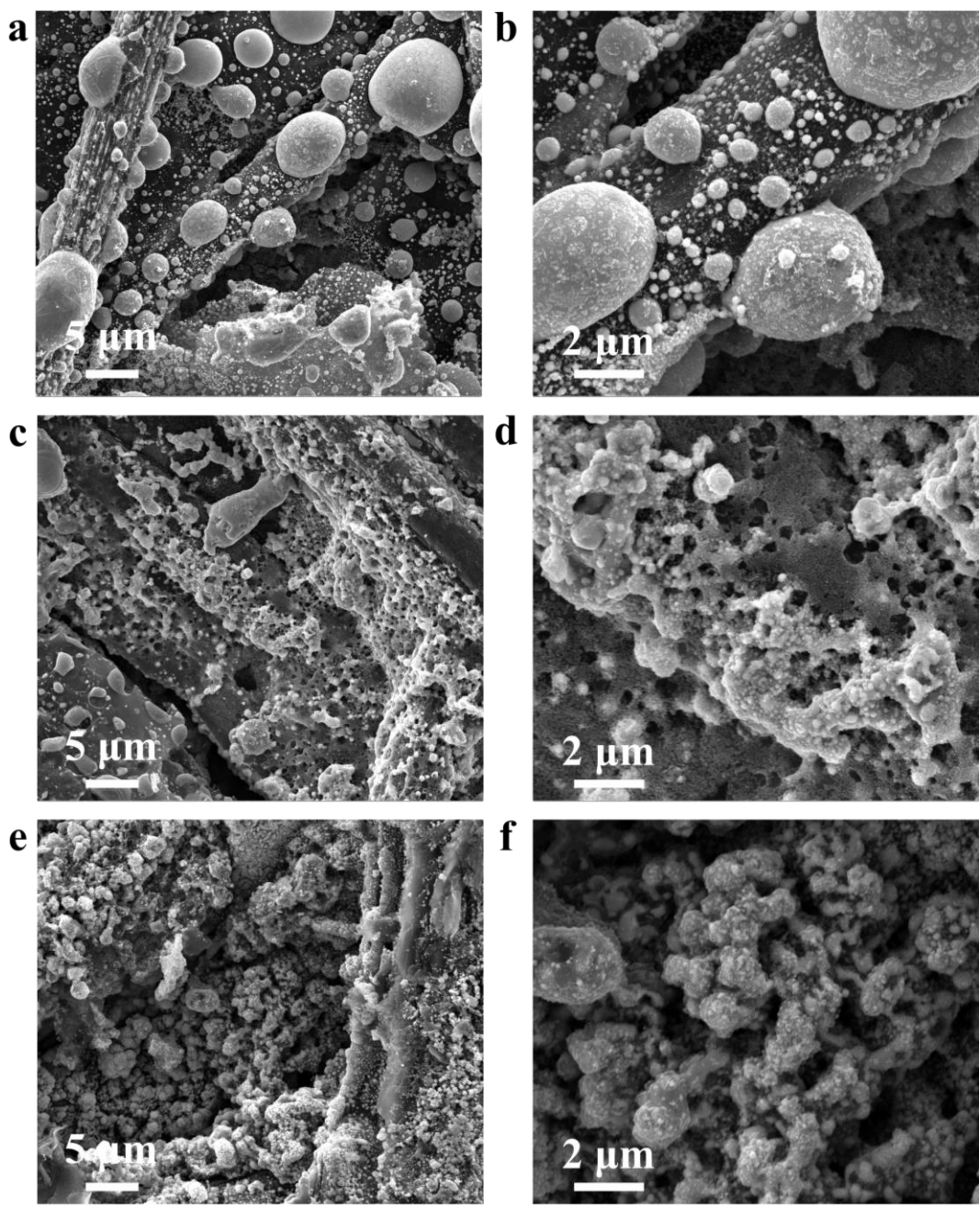


Figure S3. SEM images of (a, b) FeNiCoRu, (c, d) FeNiCoCr, and (e, f) FeNiCo.

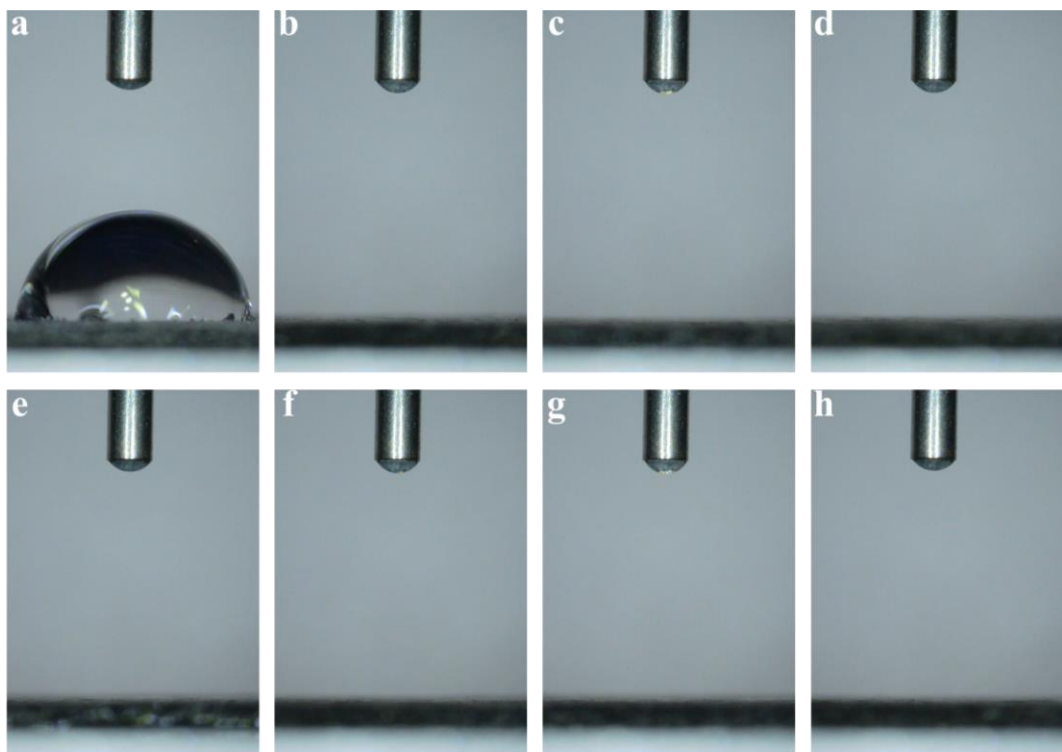


Figure S4. Surface contact angle measurements of (a) carbon paper, (b) Fe, (c) Ni, (d) FeNi, (e) FeNiCo, (f) FeNiCoCr, (g) FeNiCoRu, and (h) FeNiCoCrRu on the carbon papers.

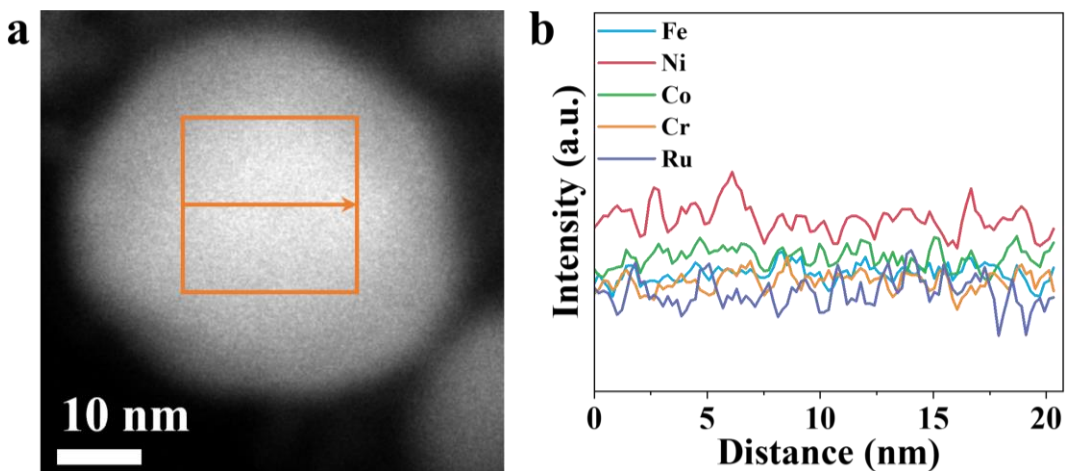


Figure S5. (a) HAADF-STEM and (b) Line-scan EDX spectra of FeNiCoCrRu.

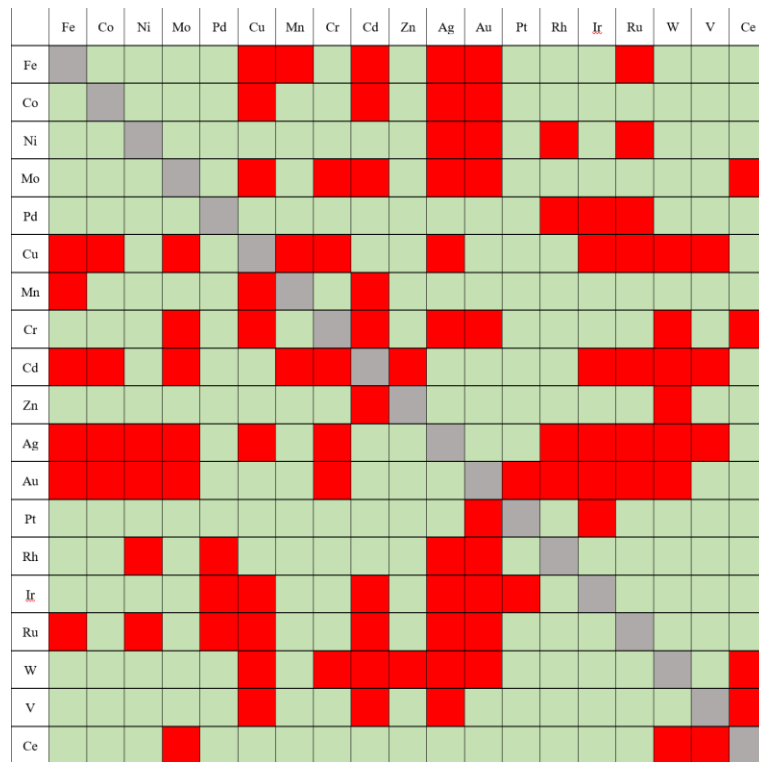


Figure S6. Miscibility maps of binary alloy systems based on 19 common metal atoms.¹⁷ The gray rectangles along the diagonal line indicate the boundary of alloys consisting of dissimilar metal atoms. The green and red rectangles represent the miscible and immiscible combinations, respectively.

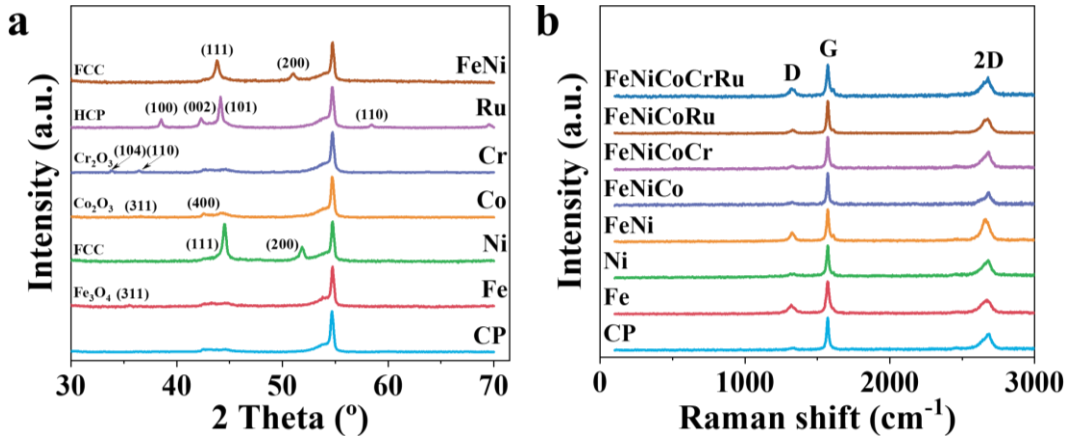


Figure S7. (a) XRD spectra of carbon paper, Fe, Ni, Co, Cr, Ru, and FeNi. (b) Raman spectra of carbon paper, Fe, Ni, FeNi, FeNiCo, FeNiCoCr, FeNiCoRu, and FeNiCoCrRu.

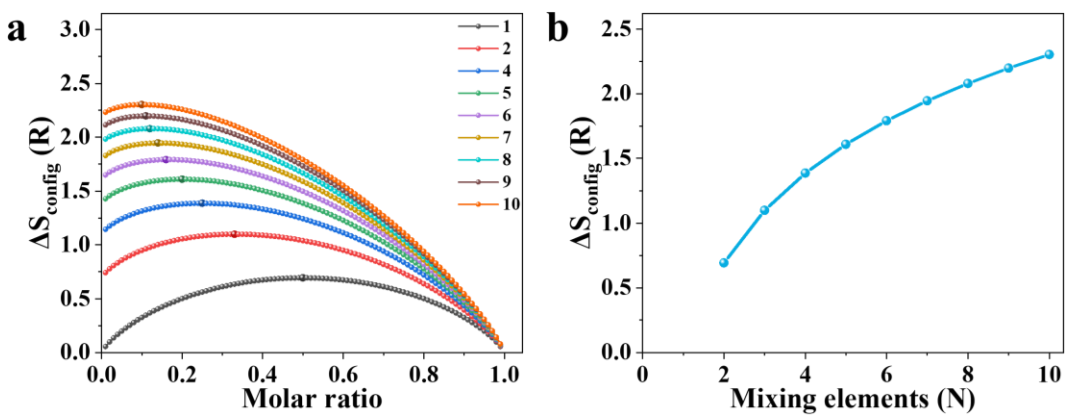


Figure S8. The relationship between the configurational entropy and (a) the molar fraction of each element; (b) the number of mixing elements.

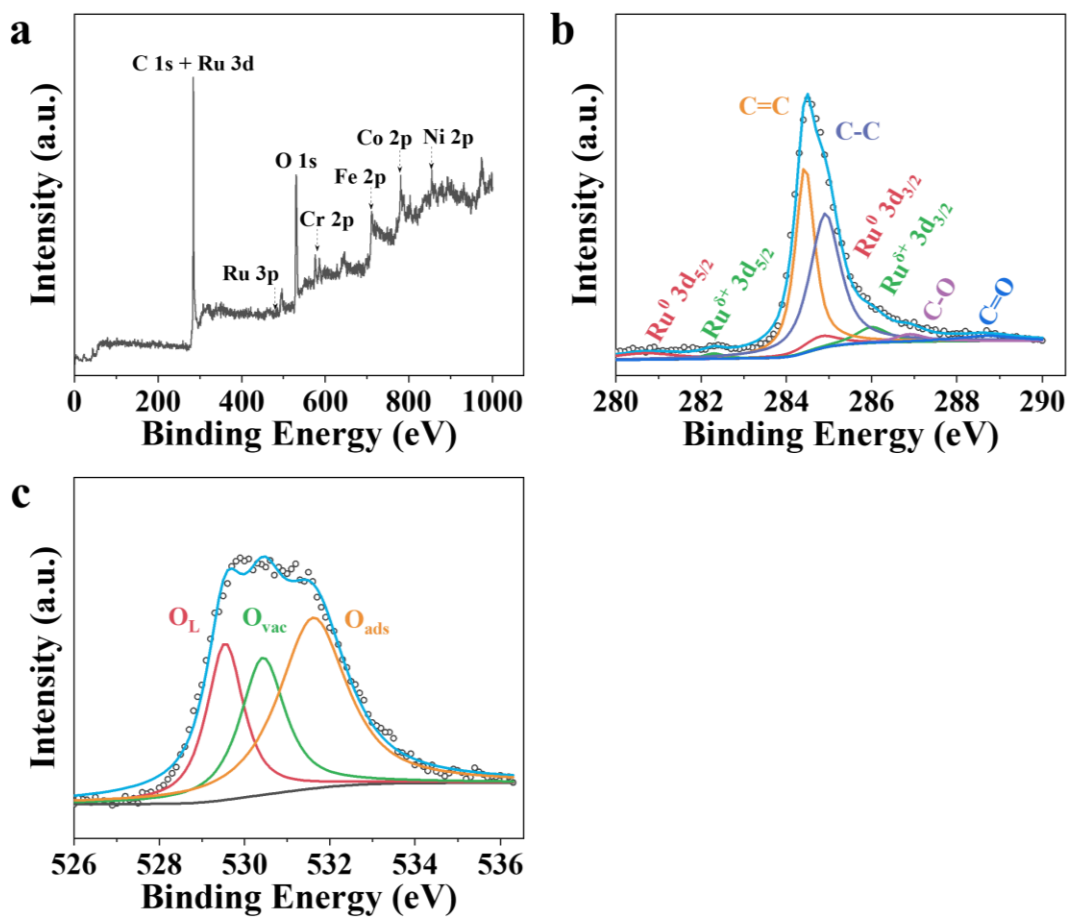


Figure S9. (a) XPS survey. High-resolution (b) C 1s and (c) O 1s spectra of FeNiCoCrRu.

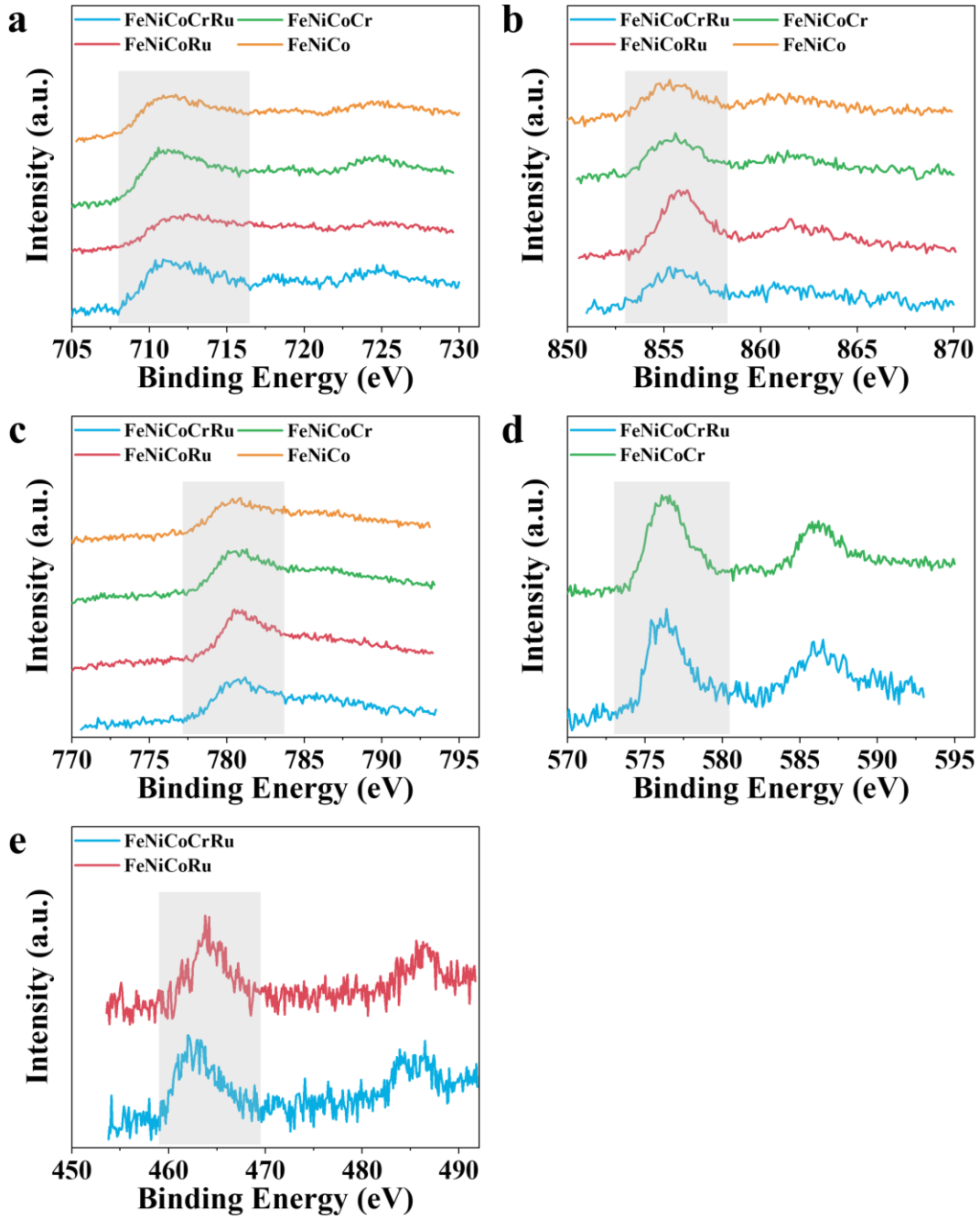


Figure S10. High-resolution of laser induced materials: (a) Fe 2p, (b) Ni 2p, and (c) Co 2p spectra of FeNiCoCrRu, FeNiCoRu, FeNiCoCr, and FeNiCo; (d) Cr 2p spectra of FeNiCoCrRu and FeNiCoCr; (e) Ru 3p spectra of FeNiCoCrRu and FeNiCoRu.

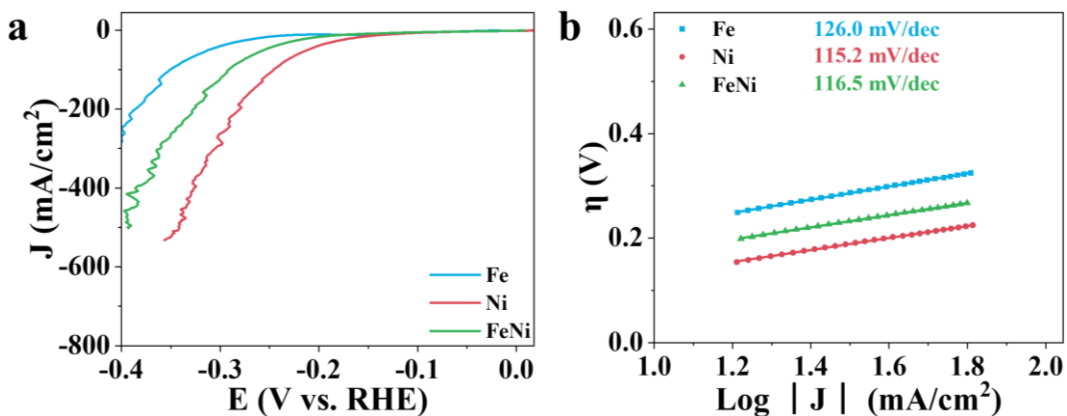


Figure S11. (a) LSV curves at a scan rate of 10 mV/s and (b) Tafel slope plots of laser induced Fe, Ni, and FeNi in 1 M KOH.

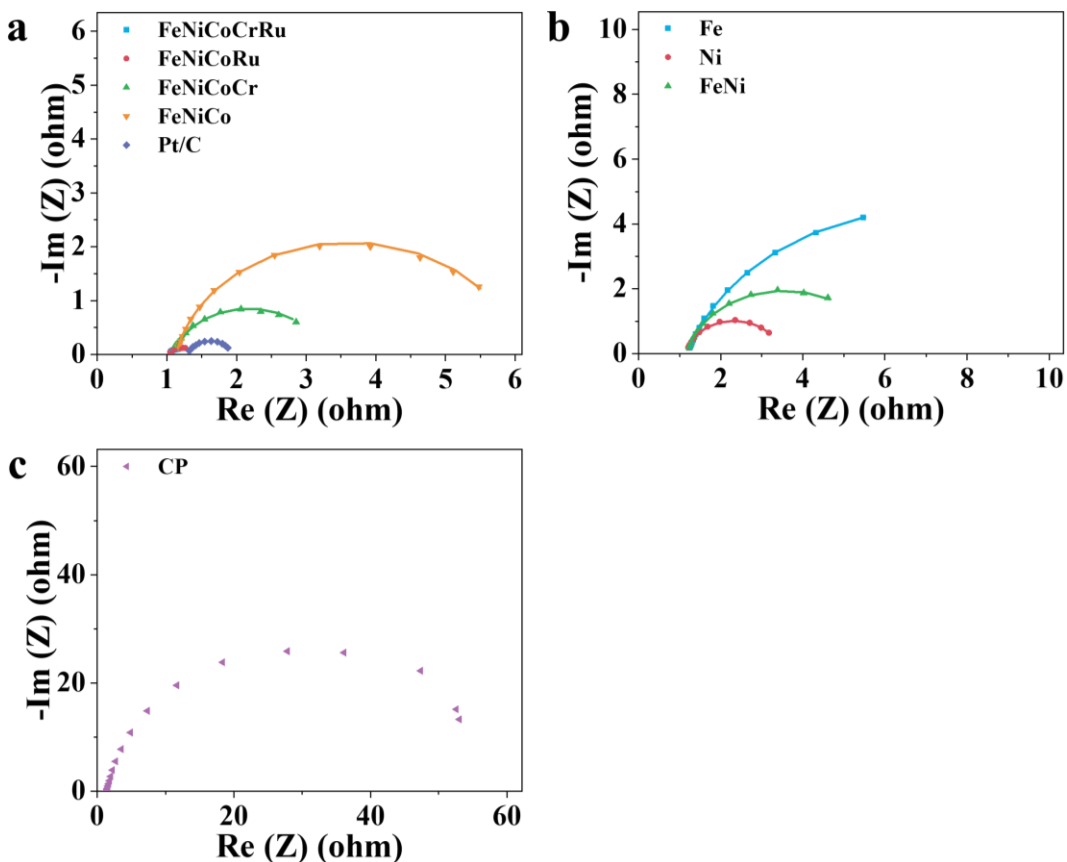


Figure S12. Nyquist plots of HER at overpotential of 0.2 V over (a) FeNiCoCrRu, FeNiCoRu, FeNiCoCr, FeNiCo and Pt/C; (b) FeNi, Ni and Fe; and (c) carbon paper in 1 M KOH.

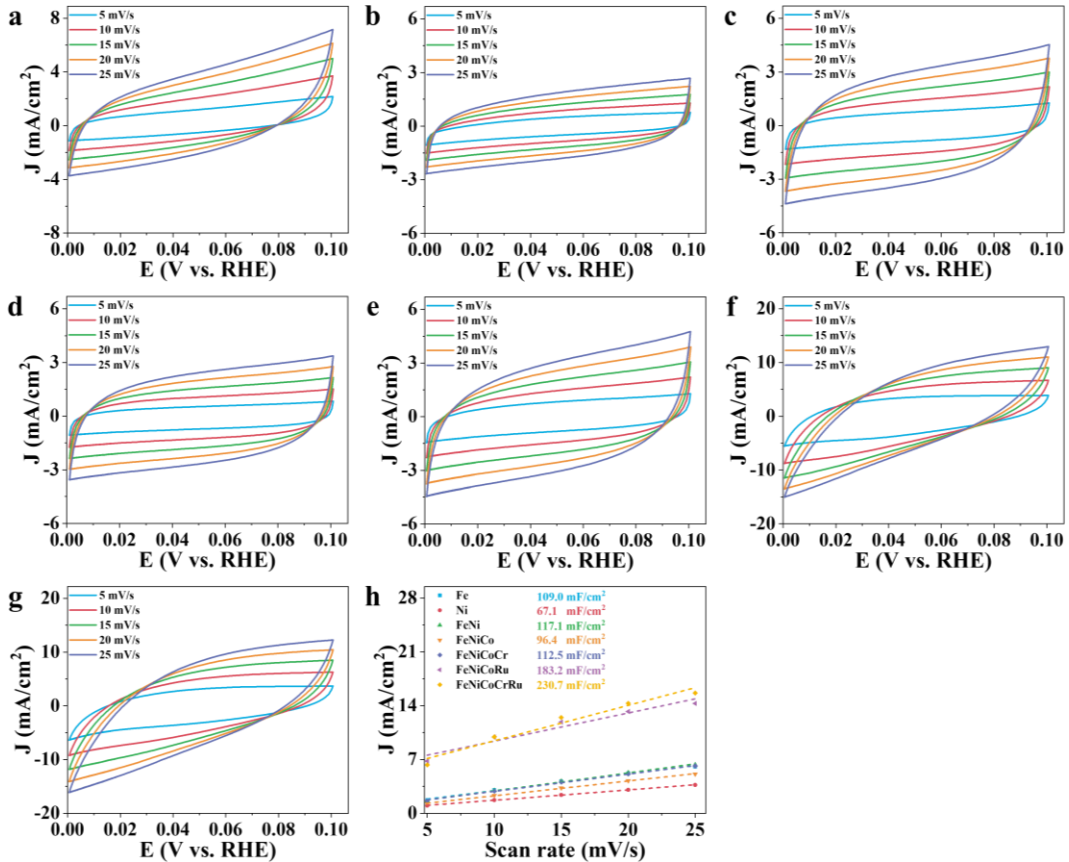


Figure S13. CV curves of laser induced materials: (a) Fe, (b) Ni, (c) FeNi, (d) FeNiCo, (e) FeNiCoCr, (f) FeNiCoRu, (g) FeNiCoCrRu electrocatalyst within 0 and 0.1 V vs RHE from 5 to 25 mV/s in 1 M KOH. (h) Plots of ΔJ ($J_a - J_c$) at potential of 0.05 V as a function of scan rates for Fe, Ni, FeNi, FeNiCo, FeNiCoCr, FeNiCoRu, and FeNiCoCrRu electrocatalysts.

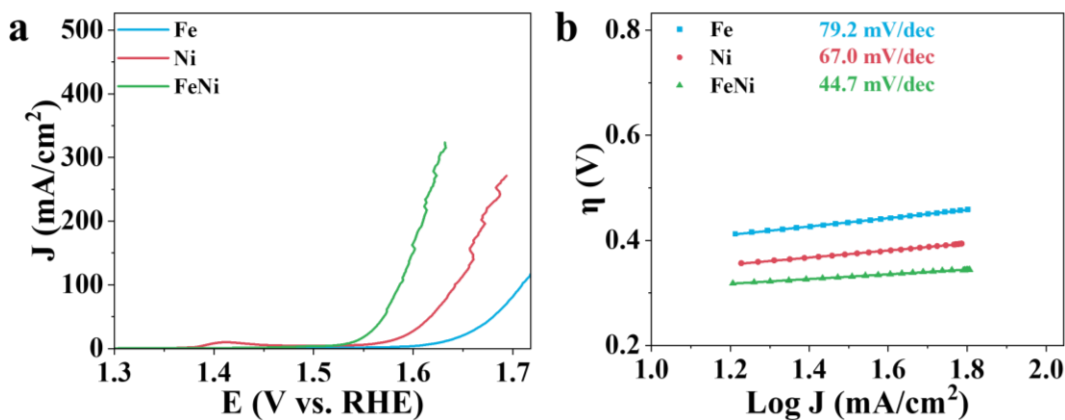


Figure S14. (a) LSV curves of OER at a scan rate of 10 mV/s and (b) Tafel slope plots of Fe, Ni, and FeNi in 1 M KOH.

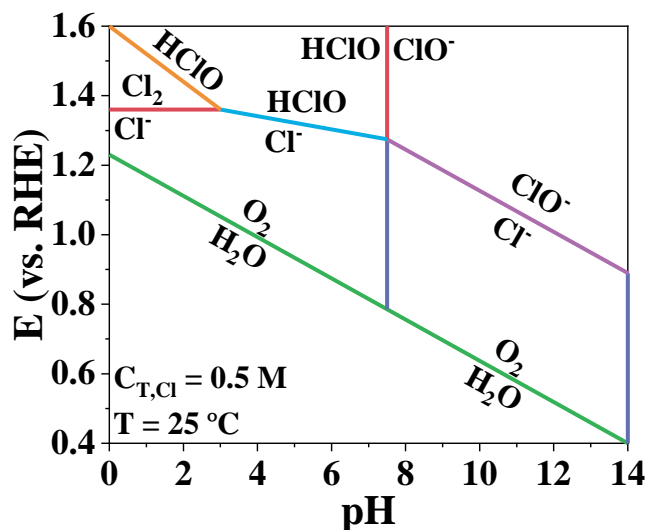


Figure S15. The Pourbaix diagram of OER and the chlorine chemistry in simulated seawater model (0.5 M NaCl) under different pH values.¹

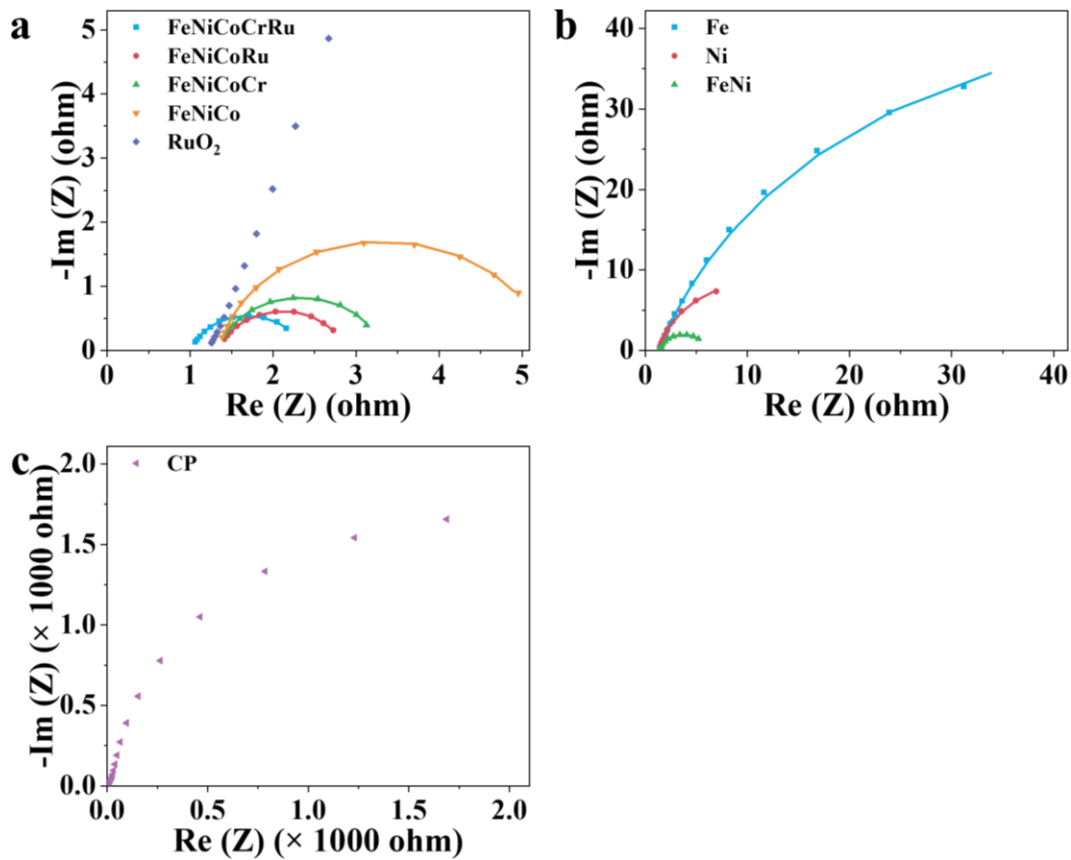


Figure S16. Nyquist plots of OER at overpotential of 0.3 V over (a) FeNiCoCrRu, FeNiCoRu, FeNiCoCr, FeNiCo and RuO₂; (b) FeNi, Ni and Fe; and (c) carbon paper in 1 M KOH.

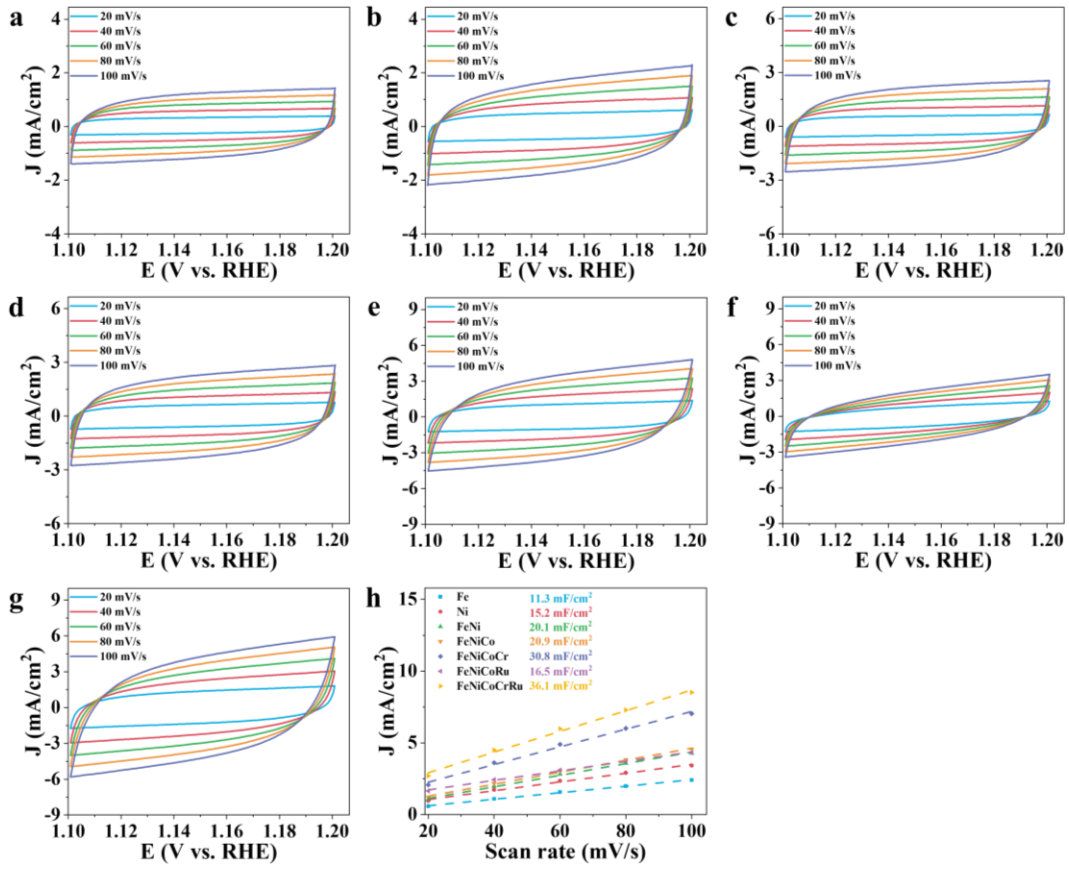


Figure S17. CV curves of (a) Fe, (b) Ni, (c) FeNi, (d) FeNiCo, (e) FeNiCoCr, (f) FeNiCoRu, (g) FeNiCoCrRu electrocatalyst within 1.0 and 1.1 V vs RHE from 20 to 100 mV/s in 1 M KOH. (h) Plots of ΔJ ($J_a - J_c$) at an overpotential of 1.05 V as a function of scan rates for Fe, Ni, FeNi, FeNiCo, FeNiCoCr, FeNiCoRu, and FeNiCoCrRu electrocatalysts.

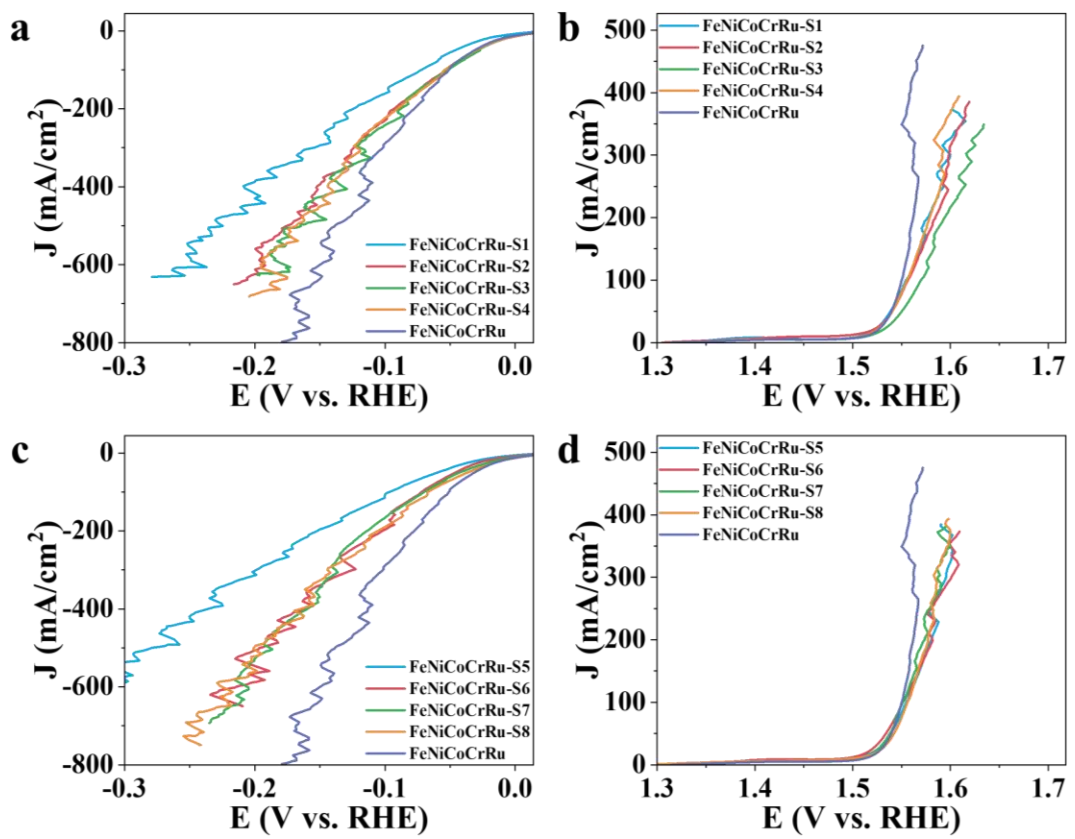


Figure S18. LSV curves of (a, c) HER and (b, d) OER over various samples under different reaction conditions.

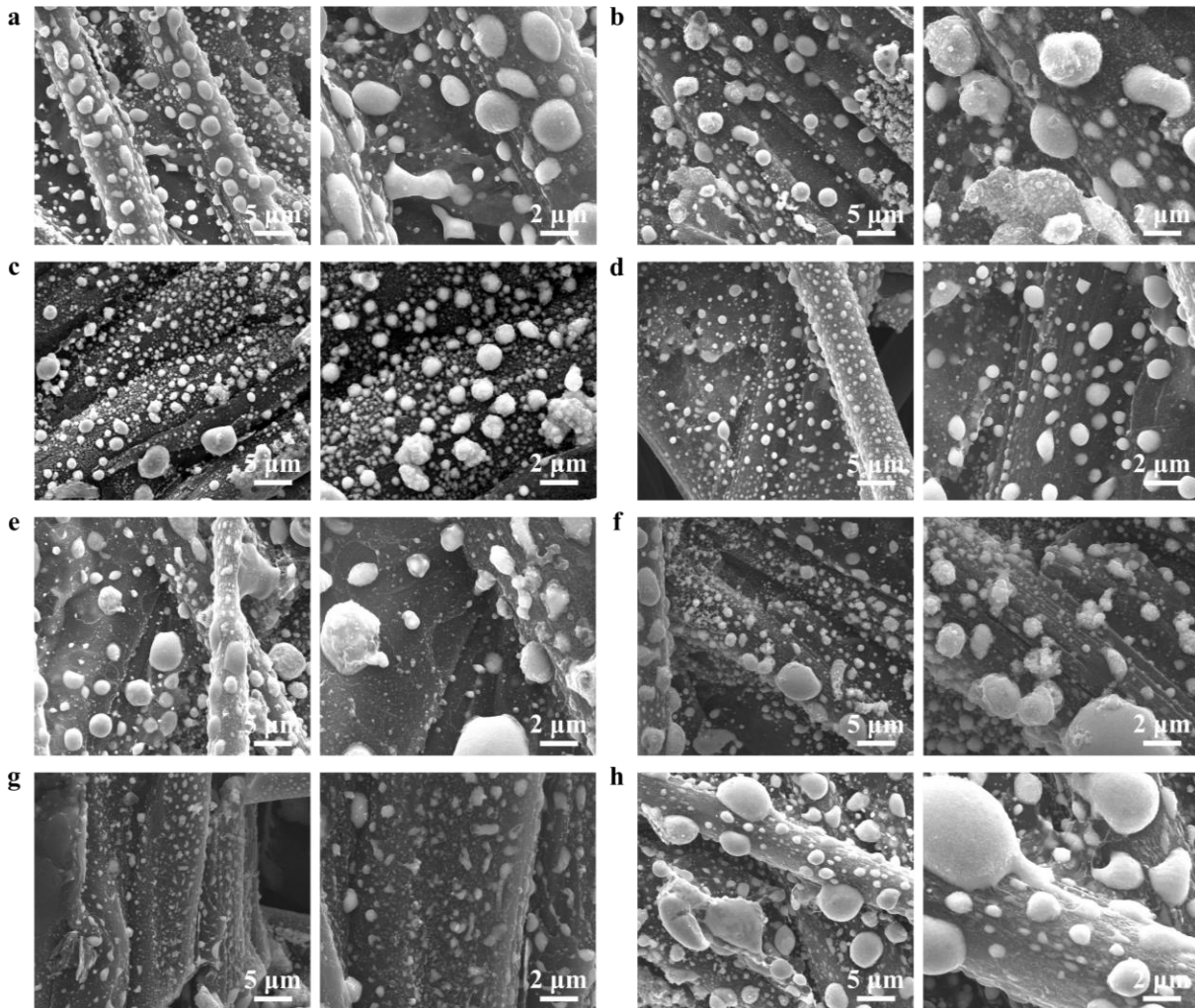


Figure S19. SEM images of (a) FeNiCoCrRu-S1, (b) FeNiCoCrRu-S2, (c) FeNiCoCrRu-S3, (d) FeNiCoCrRu-S4, (e) FeNiCoCrRu-S5, (f) FeNiCoCrRu-S6, (g) FeNiCoCrRu-S7, and (h) FeNiCoCrRu-S8.

To reveal the morphology and particle sizes of FeNiCoCrRu HEA NPs under different reaction conditions, SEM images were collected. As shown in **Fig. S19**, unlike the FeNiCoCrRu HEA NPs, these eight samples exhibit no porous structures. It is deduced that low laser power (**Fig. S19a**) results in NPs with larger size distribution due to less energy input, while fast scan rate (**Fig. S19d**) facilitates the formation of more uniform and smaller NPs due to fast decomposition of sodium citrate or shorter quenching process. Conversely, high laser power and slow scan rate concentrate

excessive energy on the carbon paper (**Fig. S19b** and **S19c**), causing complete decomposition of sodium citrate or prolonging the quenching process. This leads to the formation of larger isolated NPs. Low concentration of metal salts results in a lower density of HEA NPs (**Fig. S19e**), whereas high concentration of sodium citrate leads to HEA NPs with a wider size distribution (**Fig. S19h**). Conversely, high concentration of metal salts (**Fig. S19f**) and low concentration of sodium citrate (**Fig. S19g**) lead to HEA NPs with a more uniform size distribution. Hence, the optimal reaction conditions promote the formation of FeNiCoCrRu HEA NPs with porous structures and a smaller, more uniform size distribution, which are beneficial for electrocatalytic activity.

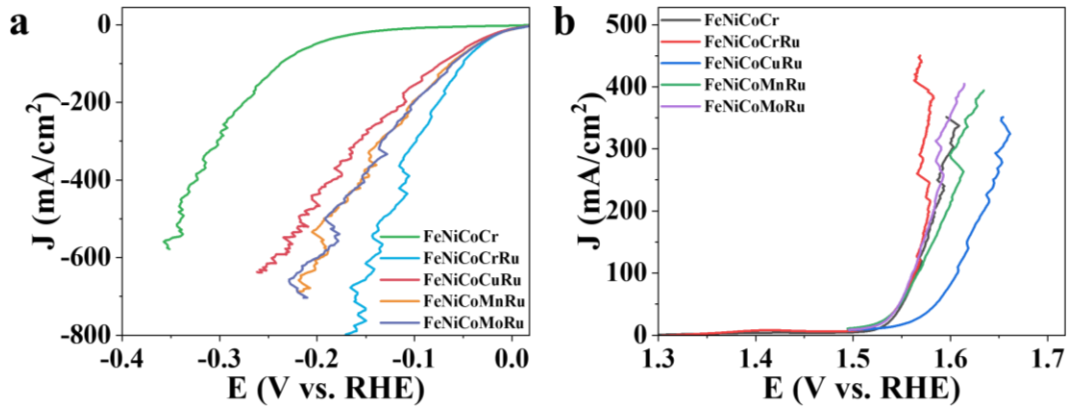


Figure S20. LSV curves of (a) HER and (b) OER over FeNiCoCr, FeNiCoCrRu, FeNiCoCuRu, FeNiCoMnRu, and FeNiCoMoRu in 1 M KOH.

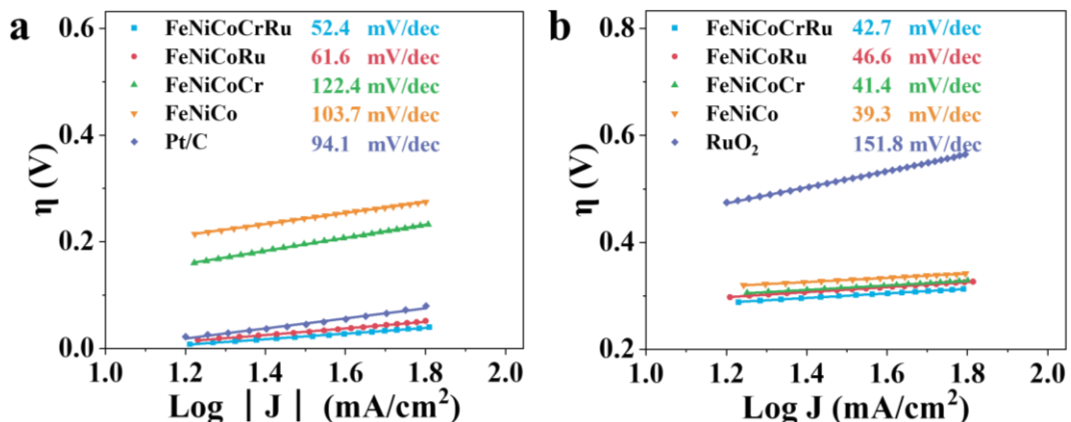


Figure S21. Tafel slope plots of (a) HER over FeNiCoCrRu, FeNiCoRu, FeNiCoCr, FeNiCo and Pt/C, and (b) OER over FeNiCoCrRu, FeNiCoRu, FeNiCoCr, FeNiCo and RuO₂ in 1 M KOH + 0.5 M NaCl.

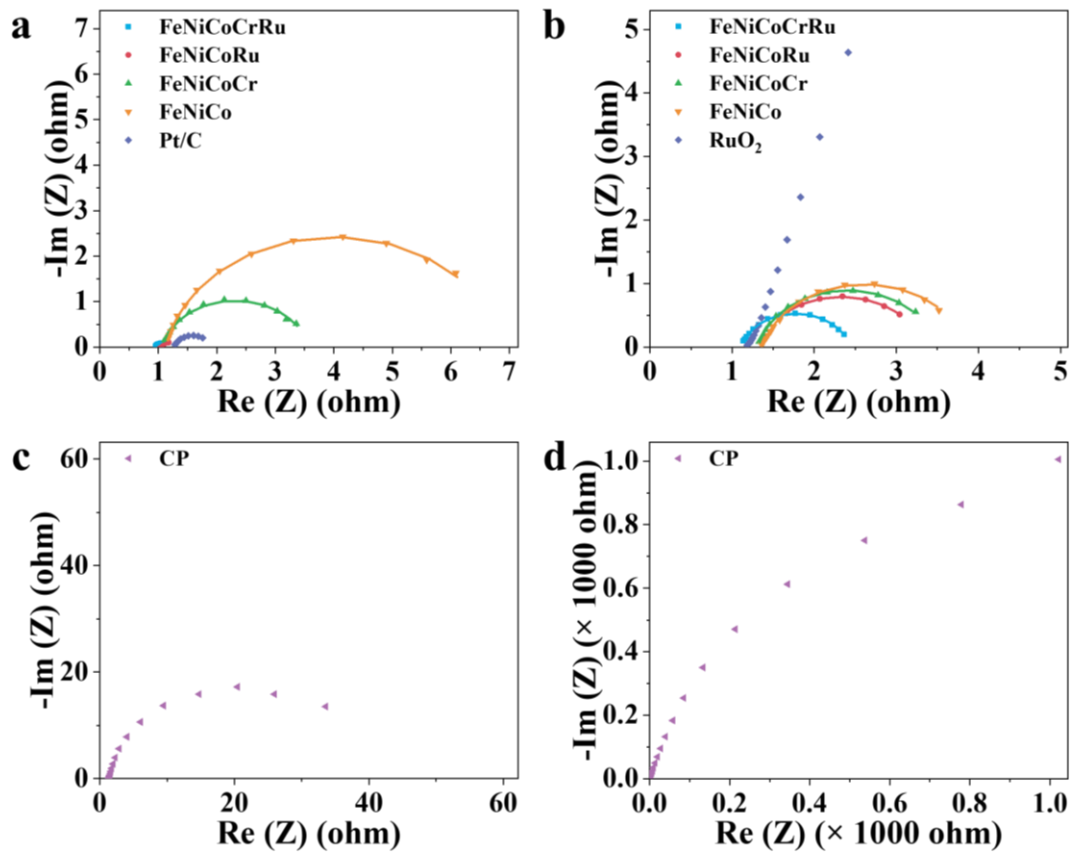


Figure S22. Nyquist plots of HER at an overpotentials of 0.2 V over (a) FeNiCoCrRu, FeNiCoRu, FeNiCoCr, FeNiCo and Pt/C and (b) carbon paper. Nyquist plots of OER at an overpotentials of 0.3 V over (c) FeNiCoCrRu, FeNiCoRu, FeNiCoCr, FeNiCo and RuO₂ and (d) carbon paper in 1 M KOH + 0.5 M NaCl.

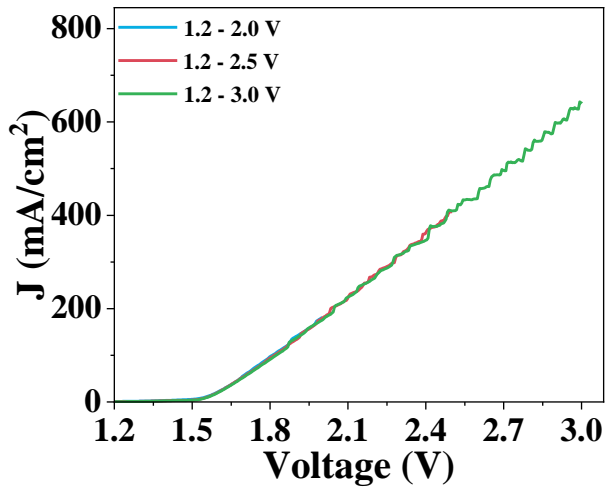


Figure S23. LSV curves of FeNiCoCrRu||FeNiCoCrRu electrolyzer without *iR*-correction under different voltage range.

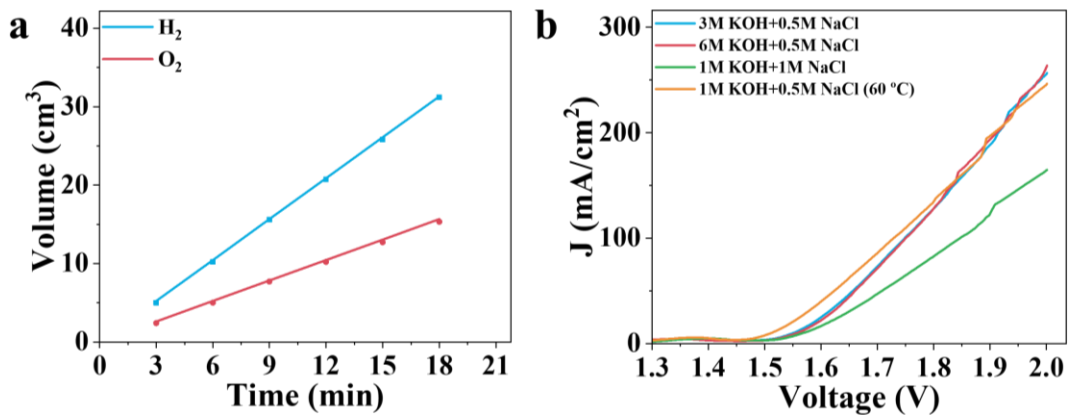


Figure S24. (a) The Faradaic efficiencies of FeNiCoCrRu electrocatalyst for H₂ and O₂ production under 1 M KOH + 0.5 M NaCl. (b) LSV curves of the FeNiCoCrRu||FeNiCoCrRu electrolyzer under the electrolyte of 1 M KOH + 1 M NaCl, 3 M KOH + 0.5 M NaCl, 6 M KOH + 0.5 M NaCl, and 1 M KOH + 0.5 M NaCl (60 °C), respectively.



Figure S25. Photograph showing seawater electrolysis of the FeNiCoCrRu||FeNiCoCrRu electrolyzer driven by a 1.5 V AA battery.

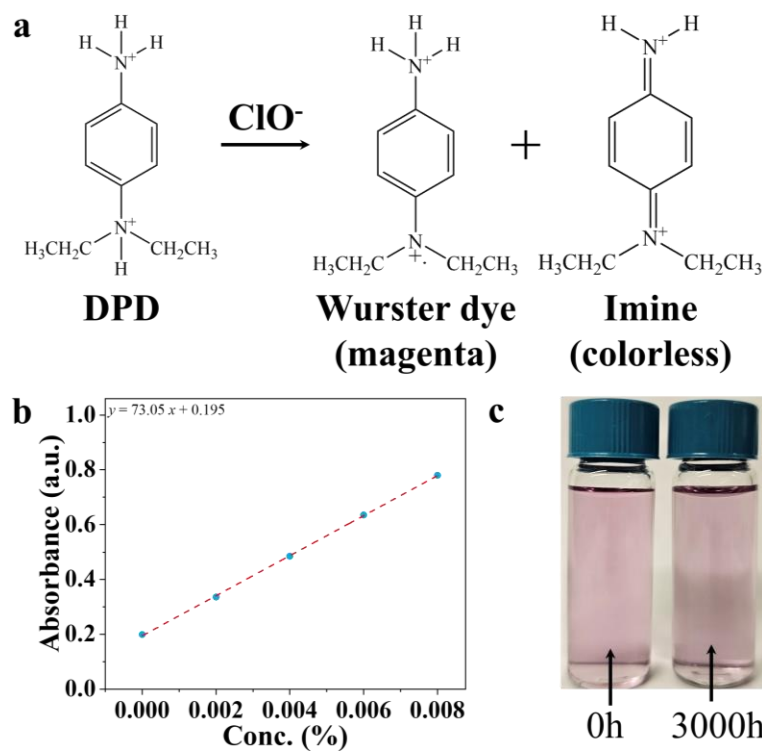


Figure S26. (a) The reaction between DPD (N,N-diethyl-p-phenylenediamine) with ClO^- . (b) Plot of absorption at various concentrations of hypochlorite. (c) Photograph showing the color change before and after long-term stability test.

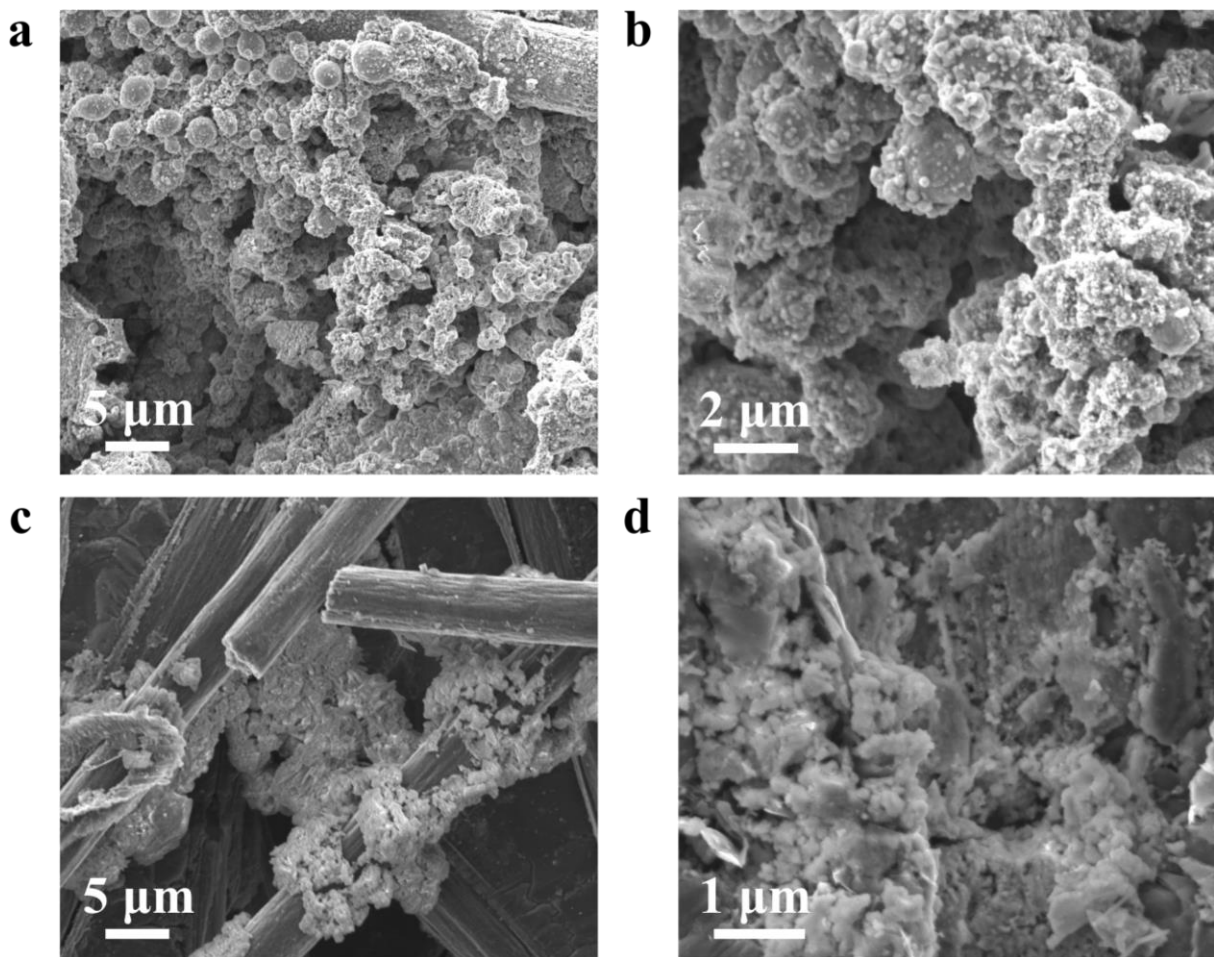


Figure S27. SEM image of FeNiCoCrRu on the (a, b) cathode (HER) and (c, d) anode (OER) after long-term stability test.

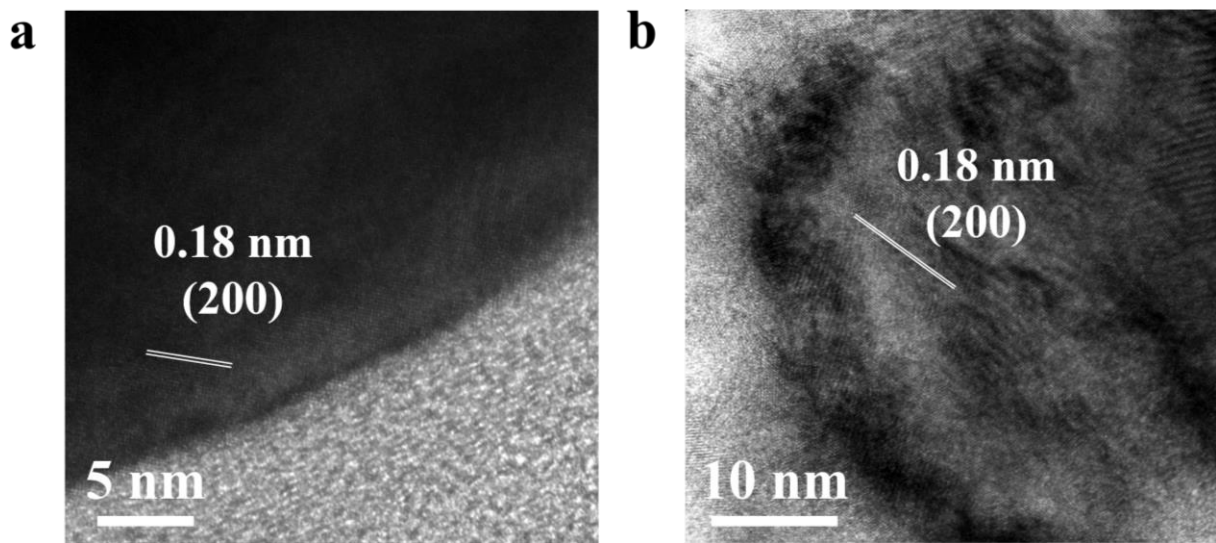


Figure S28. HRTEM images of FeNiCoCrRu on the (a) cathode (HER) and (b) anode (OER) after long-term stability test.

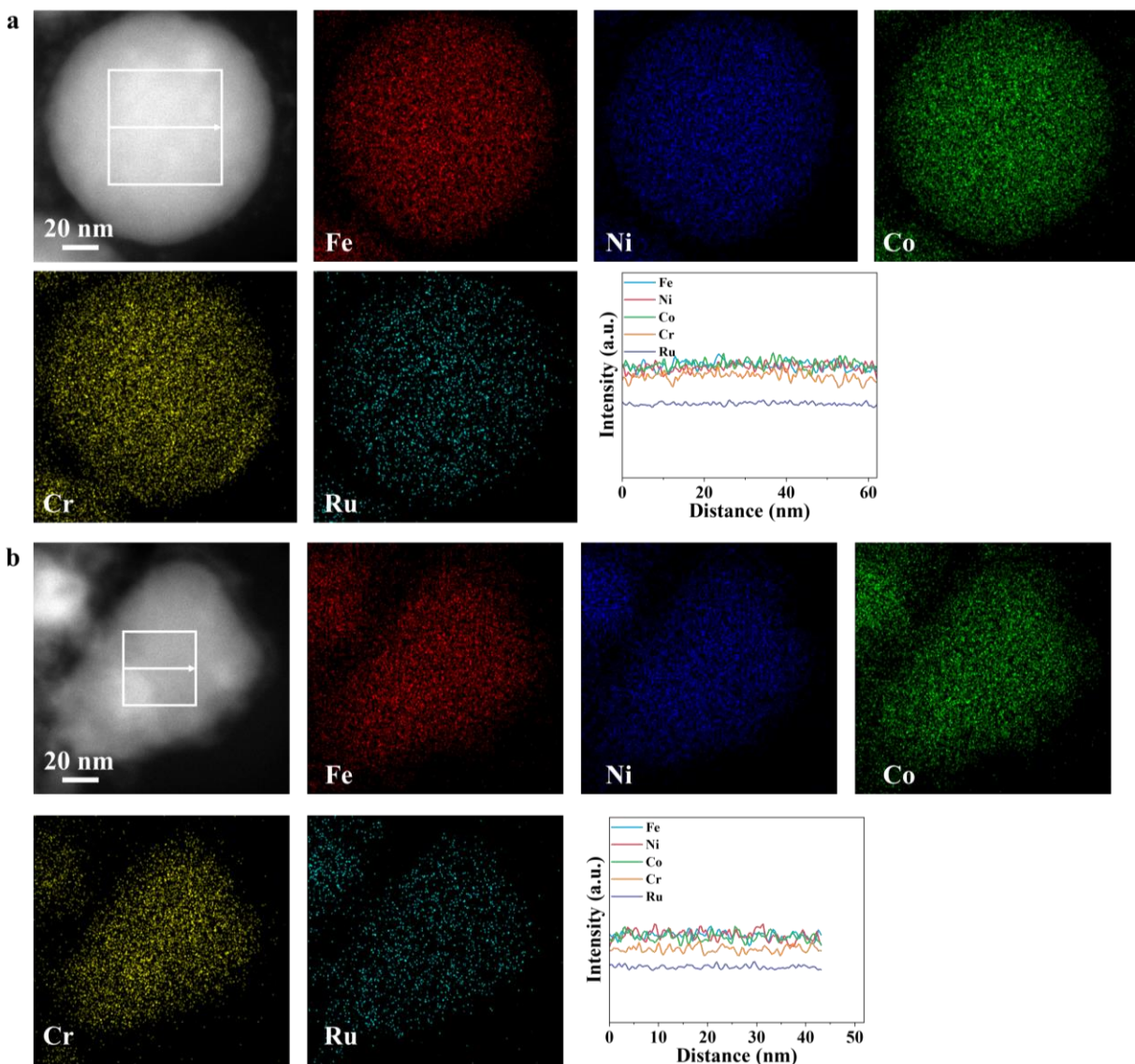


Figure S29. HAADF-STEM, EDX, and Line-scan EDX spectra of FeNiCoCrRu on the **(a)** cathode (HER) and **(b)** anode (OER) after long-term stability test.

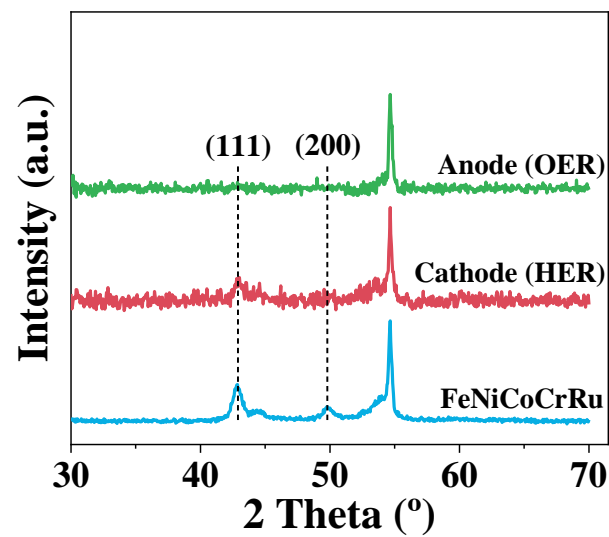


Figure S30. XRD comparison among cathode, anode, and original samples.

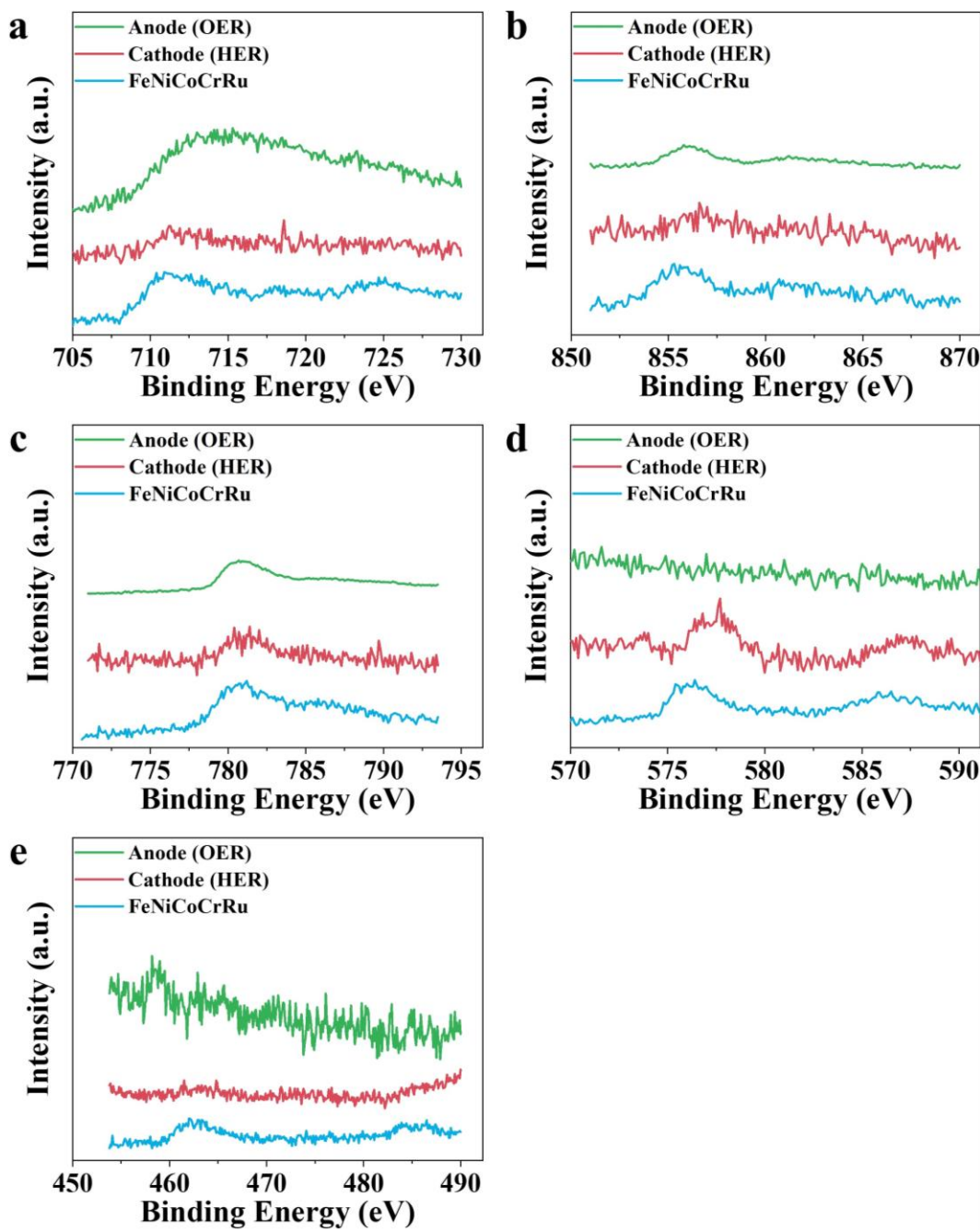


Figure S31. (a) Fe 2p, (b) Ni 2p, (c) Co 2p, (d) Cr 2p, and (e) Ru 3p spectra of FeNiCoCrRu after long-term stability test.

Supplementary Tables

Table S1. Details of metal precursor solutions.

Electrocatalysts	Metal salts (mmol)					Sodium Citrate (mmol)	H ₂ O (mL)	Ethanol (mL)	Laser	
	Fe ³⁺	Ni ²⁺	Co ²⁺	Cr ³⁺	Ru ³⁺				Power (W)	Rate (cm/s)
Fe	0.480	/	/	/	/					
Ni	/	0.480	/	/	/					
Co	/	/	0.480	/	/					
Cr	/	/	/	0.480	/					
Ru	/	/	/	/	0.480					
FeNi	0.240	0.240	/	/	/				18	10
FeNiCo	0.160	0.160	0.160	/	/					
FeNiCoCr	0.120	0.120	0.120	0.120	/					
FeNiCoRu	0.120	0.120	0.120	/	0.120					
FeNiCoCrRu	0.096	0.096	0.096	0.096	0.096					
FeNiCoCrRu-S1									12	
FeNiCoCrRu-S2									24	
FeNiCoCrRu-S3	0.096	0.096	0.096	0.096	0.096					5
FeNiCoCrRu-S4										20
FeNiCoCrRu-S5	0.048	0.048	0.048	0.048	0.048					
FeNiCoCrRu-S6	0.192	0.192	0.192	0.192	0.192					
FeNiCoCrRu-S7						0.48				
FeNiCoCrRu-S8	0.096	0.096	0.096	0.096	0.096	2.40				
FeNiCoCuRu	0.096	0.096	0.096	Cu ²⁺ 0.096	0.096				18	10
FeNiCoMnRu	0.096	0.096	0.096	Mn ²⁺ 0.096	0.096					
FeNiCoMoRu	0.096	0.096	0.096	MoO ₄ ²⁻ 0.096	0.096					

Table S2. The physical properties of metallic elements.

	T_m (K)	T_b (K)	r (nm)	Crystal structure	χ (eV)	VEC	Electron configuration
Fe	1812	3135	0.126	BCC/FCC	1.83	8	[Ar]4s ² 3d ⁶
Co	1766	3143	0.125	HCP/FCC	1.88	9	[Ar]4s ² 3d ⁸
Ni	1728	3188	0.124	FCC	1.91	10	[Ar]4s ² 3d ⁷
Cr	2180	2945	0.130	BCC	1.66	6	[Ar]4s ¹ 3d ⁵
Ru	2607	4350	0.134	HCP	2.20	8	[Kr]5s ¹ 4d ⁷
Cu	1358	2835	0.128	FCC	1.90	11	[Ar]4s ¹ 3d ¹⁰
Mn	1518	2334	0.127	BCC	1.55	7	[Ar]4s ² 3d ⁵
Mo	2896	4912	0.139	BCC	2.16	6	[Kr]5s ¹ 4d ⁵
Pd	1828	3236	0.137	FCC	2.20	10	[Kr]4d ¹⁰
Cd	592	1040	0.154	HCP	1.69	12	[Kr]5s ² 4d ¹⁰
Zn	693	1179	0.138	HCP	1.65	12	[Ar]4s ² 3d ¹⁰
Ag	1235	2435	0.144	FCC	1.93	11	[Kr]5s ¹ 4d ¹⁰
Au	1337	2973	0.144	FCC	2.54	11	[Xe]6s ¹ 4f ¹⁴ 5d ¹⁰
Pt	2041	4098	0.139	FCC	2.28	10	[Xe]6s ¹ 4f ¹⁴ 5d ⁹
Rh	2237	4000	0.134	FCC	2.28	9	[Kr]5s ¹ 4d ⁸
Ir	2683	4403	0.136	FCC	2.20	9	[Xe]6s ² 4f ¹⁴ 5d ⁷
W	3695	5828	0.141	BCC	2.36	6	[Xe]6s ² 4f ¹⁴ 5d ⁴
V	2183	3680	0.134	BCC	1.63	5	[Ar]4s ² 3d ³
Ce	1068	3716	0.181	DHCP	1.12	3	[Xe]6s ² 4f ¹ 5d ¹

Note: T_m: melting temperature, T_b: boiling temperature, r: atomic radius, χ: electronegativity, VEC: valence electron concentration.

Table S3. Mixing enthalpy ($\text{kJ}\cdot\text{mol}^{-1}$) between two transition metals.¹⁸

	Fe	Co	Ni	Cu	Mn	Ru	Mo	Cr
Fe								
Co	-1							
Ni	-2	0						
Cu	13	6	4					
Mn	0	-5	-8	4				
Ru	-5	-1	0	7	-11			
Mo	-2	-5	-7	19	5	-14		
Cr	-1	-4	-7	12	2	-12	0	

Table S4. Calculated atomic size difference (δ), electronegativity difference ($\Delta\chi$), mixing enthalpy (ΔH_{mix}), mixing entropy (ΔS_{mix}), mixing valence electron concentration (VEC_{mix}), mixing melting temperature (T_{mix}), and lattice constant (a).

	\bar{r} (nm)	δ	$\bar{\chi}$	$\Delta\chi$	ΔH_{mix} ($\text{kJ}\cdot\text{mol}^{-1}$)	ΔS_{mix} ($\text{J}\cdot\text{K}^{-1}\cdot\text{mol}^{-1}$)	VEC_{mix}	T_{mix} (K)	a (nm)
FeNi	0.125	0.8	1.870	0.040	2.00	5.763	9	1770	0.354
FeNiCo	0.125	0.653	1.873	0.033	-1.33	9.130	9	1768.6	0.354
FeNiCoRu	0.12725	3.11	1.955	0.144	-2.25	11.53	8.75	1978.3	0.360
FeNiCoCr	0.12625	1.80	1.820	0.097	-3.75	11.53	8.25	1871.5	0.357
FeNiCoCrRu	0.1278	2.90	1.896	0.175	-5.28	13.38	8.2	2018.6	0.361

Table S5. ICP-MS results of various electrocatalysts (at %).

Electrocatalysts	Elements				
	Fe	Ni	Co	Cr	Ru
FeNiCoCrRu	0.17	0.19	0.34	0.10	0.20
FeNiCoRu	0.19	0.21	0.37	/	0.23
FeNiCoCr	0.19	0.27	0.44	0.10	/
FeNiCo	0.25	0.28	0.47	/	/

Table S6. Comparison of the overpotentials at different current densities, Tafel slopes, R_s , R_{ct} , and ECSA for various electrocatalysts for HER and OER in 1.0 M KOH.

Electrocatalysts	HER												Mass Activity (A/g) at η of 0.10 V		
	η (V)@J								Tafel slope (mV/dec)	EIS (ohm)		ECSA (cm ²)			
	10	50	100	200	300	400	500	600		R_s	R_{ct}				
FeNiCoCrRu	0.002	0.032	0.051	0.078	0.102	0.113	0.139	0.150	52.2	0.993	0.477	5767.5	474.39		
FeNiCoRu	0.004	0.043	0.071	0.108	0.139	0.162	0.19	0.191	60.7	1.041	0.357	4580	221.76		
FeNiCoCr	0.112	0.203	0.238	0.275	0.303	0.324	0.340	/	122.8	1.093	2.166	2812.5	19.23		
FeNiCo	0.176	0.256	0.286	0.322	0.347	0.371	0.394	/	107.9	1.135	4.949	2410	16.29		
FeNi	0.165	0.255	0.292	0.327	0.361	0.386	0.392	/	116.5	1.173	4.74	2927.5	/		
Ni	0.126	0.211	0.247	0.281	0.305	0.327	0.341	/	115.2	1.177	2.292	1677.5	/		
Fe	0.127	0.132	0.351	0.385	0.405	0.427	/	/	126.0	1.183	11.96	2725	/		
Pt/C	0.012	0.058	0.099	0.154	0.200	0.234	0.263	/	84.5	1.303	0.653	/	194.8		
Electrocatalysts	OER												Mass Activity (A/g) at η of 0.32 V		
	η (V)@J								Tafel slope (mV/dec)	EIS (ohm)		ECSA (cm ²)			
	10	50	100	200	300	400	/	/		R_s	R_{ct}				
FeNiCoCrRu	0.285	0.310	0.321	0.331	0.332	0.329	/	/	35	1.028	1.325	902.5	167.82		
FeNiCoRu	0.280	0.312	0.327	0.349	0.359	/	/	/	40.4	1.360	1.511	412.5	108.55		
FeNiCoCr	0.295	0.321	0.336	0.353	0.372	/	/	/	36.6	1.354	1.951	770	112.78		
FeNiCo	0.300	0.328	0.346	0.369	0.379	/	/	/	41.7	1.355	3.937	522.5	17.90		
FeNi	0.308	0.341	0.357	0.380	0.396	/	/	/	44.7	1.353	4.871	502.5	/		
Ni	0.342	0.388	0.412	0.438	/	/	/	/	67	1.373	20.5	380	/		
Fe	0.4	0.45	0.48	0.511	/	/	/	/	79.2	1.309	102.1	282.5	/		
RuO₂	0.446	0.541	0.586	/	/	/	/	/	138.4	1.451	94.33	/	1.36		

Table S7. Comparison of the overpotentials at different current densities and Tafel slopes for various electrocatalysts for HER and OER in 1.0 M KOH.

Electrocatalysts	HER				OER					Ref.	
	η (V)@J				Tafel slope (mV/dec)	η (V)@J					
	10	100	200	500		10	100	200	400		
FeNiCoCrRu	0.002	0.051	0.078	0.139	52.2	0.285	0.321	0.331	0.329	35	
Pt₂₈Mo₆Pd₂₈Rh₂₇Ni₁₅	0.010	0.058			25.9					19	
FeCoNiCuMn/CNF		0.281			53			0.386		69	
(FeCoNiB_{0.75})₉₇Pt₃	0.027			0.091	30.9	0.170			0.287	37.8	
H-FeCoNiCuMo	0.007			0.100	19.4	0.194			0.284	34.7	
FeCoNiMnRu/CNFs	0.005	0.071			67.4	0.145	0.308			67.4	
FeCoNiCuPtIr@CNT	0.021				54.5	0.255				61.7	
Co_{0.6}(VMnNiZn)_{0.4}PS₃	0.066				65.5					25	
FeCoNiCuPd	0.030				47.2	0.194			39.8	26	
FeCoPdIrPt@GO	0.042				82					27	
MoC₂/MoC/C		0.160	0.175		42					28	
FeP-CoP/NC		0.160	0.220		71					29	
Co₇Mo₆		0.080	0.140		46					30	
NiCo/NC		0.189	0.245		55					31	
W-NiS_{0.5}Se_{0.5}		0.106	0.120		51					32	
(Fe,Co)OOH/MI					0.230				73	33	
(Ni₇Fe₃)OOH-S					0.238				42.7	34	
(CrFeCoNiMo)₃O₄					0.255				37	35	
(CrFeCoNi)₉₇O₃					0.196				29	36	
FeNiCoCrMnS₂					0.199				39.1	37	
FeCoNiMnCu					0.28				59	38	

Table S8. Comparison of the overpotentials at different current densities, Tafel slopes, R_s and R_{ct} for various electrocatalysts for HER and OER in 1.0 M KOH + 0.5 M NaCl.

Electrocatalysts	HER									EIS (ohm)	
	η (V) @ J								Tafel slope (mV/dec)		
	10	50	100	200	300	400	500	600	R_s	R_{ct}	
FeNiCoCrRu	0.002	-0.035	-0.052	-0.081	-0.102	-0.109	-0.132	-0.148	52.4	0.943	0.322
FeNiCoRu	-0.006	-0.044	-0.073	-0.103	-0.141	-0.165	-0.192	-0.222	61.6	1.018	0.350
FeNiCoCr	-0.132	-0.221	-0.255	-0.293	-0.332	-0.339	-0.364	/	122.4	1.068	2.5
FeNiCo	-0.191	-0.266	-0.294	-0.328	-0.350	-0.366	-0.391	/	103.7	1.128	5.769
Pt/C	-0.013	-0.066	-0.110	-0.142	-0.226	-0.267	-0.313	/	94.1	1.275	0.613
Electrocatalysts	OER									EIS (ohm)	
	η (V) @ J								Tafel slope (mV/dec)		
	10	50	100	200	300	/	/	/	R_s	R_{ct}	
FeNiCoCrRu	0.275	0.308	0.320	0.351	0.353	/	/	/	42.7	0.8943	2.609
FeNiCoRu	0.285	0.321	0.335	0.361	0.373	/	/	/	46.6	1.312	2.033
FeNiCoCr	0.295	0.324	0.340	0.366	0.377	/	/	/	41.4	1.320	2.170
FeNiCo	0.312	0.338	0.350	0.376	0.381	/	/	/	39.3	1.370	2.490
RuO₂	0.450	0.549	0.606	/	/	/	/	/	151.8	1.241	122.6

Table S9. Comparison of FeNiCoCrRu||FeNiCoCrRu electrolyzer and recent bifunctional electrolyzers in 1.0 M KOH + 0.5 M NaCl.

Samples	Voltage (V) @ J				Ref.
	10	20	50	100	
FeNiCoCrRu	1.548	1.594	1.683	1.808	This work
NiMoN@NiFeN				1.564	³⁹
NiCoP/NiCo-LDH			1.6	1.7	⁴⁰
R-CoC₂O₄@MXene	1.52				⁴¹
Cu₂O-NF	1.71				⁴²
Ni₃S₂/Co₃S₄				1.72	⁴³
HCl-c-NiFe				1.62	⁴⁴
CuS-SVs-Ni-Co				1.61	⁴⁵
NiFe LDH/FeOOH		1.58		1.82	⁴⁶
GO@Fe@Ni-Co@NF					⁴⁷
NF/NiFe LDH	1.47			1.543	⁴⁸
S-NiMoO₄@NiFe-LDH				1.68	⁴⁹
CoB@MOF@CC	1.49				⁵⁰
NiCo(HPO₄)₂@Ni₃N/NF				1.87	⁵¹

Table S10. ICP-MS detection of metal ions concentration in the electrolyte before/after the long-term stability test over FeNiCoCrRu electrocatalyst.

	Conc. (mg/L)				
	Fe ³⁺	Ni ²⁺	Co ²⁺	Cr ³⁺	Ru ³⁺
Before	0	0	0	0	0
After	0.45	0.10	0.13	0.40	0.15

Table S11. ICP-MS results of FeNiCoCrRu after long-term stability (at %).

Electrocatalysts	Elements				
	Fe	Ni	Co	Cr	Ru
FeNiCoCrRu	0.17	0.19	0.34	0.10	0.20
Cathode (HER)	0.13	0.26	0.24	0.10	0.27
Anode (OER)	0.12	0.37	0.36	0.05	0.10

References

1. F. Dionigi, T. Reier, Z. Pawolek, M. Gliech and P. Strasser, *ChemSusChem*, 2016, **9**, 962-972.
2. M. Ning, F. Zhang, L. Wu, X. Xing, D. Wang, S. Song, Q. Zhou, L. Yu, J. Bao, S. Chen and Z. Ren, *Energy Environ. Sci.*, 2022, **15**, 3945-3957.
3. S. Dresp, F. Dionigi, M. Klingenhof and P. Strasser, *ACS Energy Lett.*, 2019, **4**, 933-942.
4. J. N. Hausmann, R. Schlögl, P. W. Menezes and M. Driess, *Energy Environ. Sci.*, 2021, **14**, 3679-3685.
5. Y. Zheng and S.-Z. Qiao, *Joule*, 2023, **7**, 20-22.
6. P. Farràs, P. Strasser and A. J. Cowan, *Joule*, 2021, **5**, 1921-1923.
7. L. Li, G. Chen, Z. Shao and H. Huang, *Energy Environ. Sci.*, 2023, **16**, 4994-5002.
8. H. Jin, J. Xu, H. Liu, H. Shen, H. Yu, M. Jaroniec, Y. Zheng and S.-Z. Qiao, *Sci. Adv.*, 2023, **9**, eadi7755.
9. H. Saada, B. Fabre, G. Loget and G. Benoit, *ACS Energy Lett.*, 2024, **9**, 3351-3368.
10. J. Guo, Y. Zheng, Z. Hu, C. Zheng, J. Mao, K. Du, M. Jaroniec, S.-Z. Qiao and T. Ling, *Nat. Energy*, 2023, **8**, 264-272.
11. H. Hu, Z. Zhang, L. Liu, X. Che, J. Wang, Y. Zhu, J. P. Attfield and M. Yang, *Sci. Adv.*, 2024, **10**, eadn7012.
12. R. Fan, C. Liu, Z. Li, H. Huang, J. Feng, Z. Li and Z. Zou, *Nat. Sustain.*, 2024, **7**, 158-167.
13. T. Li, B. Wang, Y. Cao, Z. Liu, S. Wang, Q. Zhang, J. Sun and G. Zhou, *Nat. Commun.*, 2024, **15**, 6173.
14. H. Xie, Z. Zhao, T. Liu, Y. Wu, C. Lan, W. Jiang, L. Zhu, Y. Wang, D. Yang and Z. Shao, *Nature*, 2022, **612**, 673-678.
15. T. Liu, Z. Zhao, W. Tang, Y. Chen, C. Lan, L. Zhu, W. Jiang, Y. Wu, Y. Wang, Z. Yang, D. Yang, Q. Wang, L. Luo, T. Liu and H. Xie, *Nat. Commun.*, 2024, **15**, 5305.
16. D. J. Lampert, H. Cai and A. Elgowainy, *Energy Environ. Sci.*, 2016, **9**, 787-802.
17. R. F. Zhang, X. F. Kong, H. T. Wang, S. H. Zhang, D. Legut, S. H. Sheng, S. Srinivasan, K. Rajan and T. C. Germann, *Sci. Rep.*, 2017, **7**, 9577.
18. A. Takeuchi and A. Inoue, *Mater. Trans.*, 2005, **46**, 2817-2829.
19. M. Wei, Y. Sun, J. Zhang, F. Ai, S. Xi and J. Wang, *Energy Environ. Sci.*, 2023, **16**, 4009-4019.
20. H. Zhu, S. Sun, J. Hao, Z. Zhuang, S. Zhang, T. Wang, Q. Kang, S. Lu, X. Wang, F. Lai, T. Liu, G. Gao, M. Du and D. Wang, *Energy Environ. Sci.*, 2023, **16**, 619-628.
21. X. Zhang, Y. Yang, Y. Liu, Z. Jia, Q. Wang, L. Sun, L.-C. Zhang, J. J. Krizic, J. Lu and B. Shen, *Adv. Mater.*, 2023, **35**, 2303439.
22. C.-L. Huang, Y.-G. Lin, C.-L. Chiang, C.-K. Peng, D. Senthil Raja, C.-T. Hsieh, Y.-A. Chen, S.-Q. Chang, Y.-X. Yeh and S.-Y. Lu, *Appl. Catal. B Environ.*, 2023, **320**, 122016.
23. J. Hao, Z. Zhuang, K. Cao, G. Gao, C. Wang, F. Lai, S. Lu, P. Ma, W. Dong, T. Liu, M. Du and H. Zhu, *Nat. Commun.*, 2022, **13**, 2662.
24. Y. Lu, K. Huang, X. Cao, L. Zhang, T. Wang, D. Peng, B. Zhang, Z. Liu, J. Wu, Y. Zhang, C. Chen and Y. Huang, *Adv. Funct. Mater.*, 2022, **32**, 2110645.
25. R. Wang, J. Huang, X. Zhang, J. Han, Z. Zhang, T. Gao, L. Xu, S. Liu, P. Xu and B. Song, *ACS Nano*, 2022, **16**, 3593-3603.
26. S. Wang, B. Xu, W. Huo, H. Feng, X. Zhou, F. Fang, Z. Xie, J. K. Shang and J. Jiang, *Appl. Catal. B Environ.*, 2022, **313**, 121472.

27. S. Gao, S. Hao, Z. Huang, Y. Yuan, S. Han, L. Lei, X. Zhang, R. Shahbazian-Yassar and J. Lu, *Nat. Commun.*, 2020, **11**, 2016.
28. C. Li, Z. Wang, M. Liu, E. Wang, B. Wang, L. Xu, K. Jiang, S. Fan, Y. Sun, J. Li and K. Liu, *Nat. Commun.*, 2022, **13**, 3338.
29. X. Yan, J. Biemolt, K. Zhao, Y. Zhao, X. Cao, Y. Yang, X. Wu, G. Rothenberg and N. Yan, *Nat. Commun.*, 2021, **12**, 4143.
30. R. Song, J. Han, M. Okugawa, R. Belosludov, T. Wada, J. Jiang, D. Wei, A. Kudo, Y. Tian, M. Chen and H. Kato, *Nat. Commun.*, 2022, **13**, 5157.
31. A. Kumar, V. Q. Bui, J. Lee, L. Wang, A. R. Jadhav, X. Liu, X. Shao, Y. Liu, J. Yu, Y. Hwang, H. T. D. Bui, S. Ajmal, M. G. Kim, S.-G. Kim, G.-S. Park, Y. Kawazoe and H. Lee, *Nat. Commun.*, 2021, **12**, 6766.
32. Y. Wang, X. Li, M. Zhang, J. Zhang, Z. Chen, X. Zheng, Z. Tian, N. Zhao, X. Han, K. Zaghib, Y. Wang, Y. Deng and W. Hu, *Adv. Mater.*, 2022, **34**, 2107053.
33. W. Huang, J. Li, X. Liao, R. Lu, C. Ling, X. Liu, J. Meng, L. Qu, M. Lin, X. Hong, X. Zhou, S. Liu, Y. Zhao, L. Zhou and L. Mai, *Adv. Mater.*, 2022, **34**, 2200270.
34. W. Liu, X. Wang, F. Wang, X. Liu, Y. Zhang, W. Li, Y. Guo, H. Yin and D. Wang, *Chem. Eng. J.*, 2023, **454**, 140030.
35. W. Hooch Antink, S. Lee, H. S. Lee, H. Shin, T. Y. Yoo, W. Ko, J. Shim, G. Na, Y.-E. Sung and T. Hyeon, *Adv. Funct. Mater.*, 2024, **34**, 2309438.
36. Z.-J. Chen, T. Zhang, X.-Y. Gao, Y.-J. Huang, X.-H. Qin, Y.-F. Wang, K. Zhao, X. Peng, C. Zhang, L. Liu, M.-H. Zeng and H.-B. Yu, *Adv. Mater.*, 2021, **33**, 2101845.
37. T. X. Nguyen, Y.-H. Su, C.-C. Lin and J.-M. Ting, *Adv. Funct. Mater.*, 2021, **31**, 2106229.
38. K. Huang, D. Peng, Z. Yao, J. Xia, B. Zhang, H. Liu, Z. Chen, F. Wu, J. Wu and Y. Huang, *Chem. Eng. J.*, 2021, **425**, 131533.
39. L. Yu, Q. Zhu, S. Song, B. McElhenny, D. Wang, C. Wu, Z. Qin, J. Bao, Y. Yu, S. Chen and Z. Ren, *Nat. Commun.*, 2019, **10**, 5106.
40. Y. Wu, Z. Tian, S. Yuan, Z. Qi, Y. Feng, Y. Wang, R. Huang, Y. Zhao, J. Sun, W. Zhao, W. Guo, J. Feng and J. Sun, *Chem. Eng. J.*, 2021, **411**, 128538.
41. L. Wang, Y. Hao, L. Deng, F. Hu, S. Zhao, L. Li and S. Peng, *Nat. Commun.*, 2022, **13**, 5785.
42. H. Wang, J. Ying, Y.-X. Xiao, J.-B. Chen, J.-H. Li, Z.-Z. He, H.-J. Yang and X.-Y. Yang, *Electrochem. Commun.*, 2022, **134**, 107177.
43. C. Wang, M. Zhu, Z. Cao, P. Zhu, Y. Cao, X. Xu, C. Xu and Z. Yin, *Appl. Catal. B Environ.*, 2021, **291**, 120071.
44. S. Duan, Z. Liu, H. Zhuo, T. Wang, J. Liu, L. Wang, J. Liang, J. Han, Y. Huang and Q. Li, *Nanoscale*, 2020, **12**, 21743-21749.
45. X. H. Wang, Y. Ling, B. Wu, B. L. Li, X. L. Li, J. L. Lei, N. B. Li and H. Q. Luo, *Nano Energy*, 2021, **87**, 106160.
46. K. Jiang, W. Liu, W. Lai, M. Wang, Q. Li, Z. Wang, J. Yuan, Y. Deng, J. Bao and H. Ji, *Inorg. Chem.*, 2021, **60**, 17371-17378.
47. A. R. Jadhav, A. Kumar, J. Lee, T. Yang, S. Na, J. Lee, Y. Luo, X. Liu, Y. Hwang, Y. Liu and H. Lee, *J. Mater. Chem. A*, 2020, **8**, 24501-24514.
48. M. Ning, L. Wu, F. Zhang, D. Wang, S. Song, T. Tong, J. Bao, S. Chen, L. Yu and Z. Ren, *Mater. Today Phys.*, 2021, **19**, 100419.
49. H. Wang, L. Chen, L. Tan, X. Liu, Y. Wen, W. Hou and T. Zhan, *J. Colloid Interface Sci.*, 2022, **613**, 349-358.

50. J. Fan, C. Fu, R. Liang, H. Lv, C. Fang, Y. Guo and W. Hao, *Small*, 2022, **18**, 2203588.
51. H. Sun, J. Sun, Y. Song, Y. Zhang, Y. Qiu, M. Sun, X. Tian, C. Li, Z. Lv and L. Zhang, *ACS Appl. Mater. Interfaces*, 2022, **14**, 22061-22070.